

Copyright

by

Deirdre Marie Shoemaker

1999

Apparent Horizons in Binary Black Hole Spacetimes

by

Deirdre Marie Shoemaker, B. S.

Dissertation

Presented to the Faculty of the Graduate School of

The University of Texas at Austin

in Partial Fulfillment

of the Requirements

for the Degree of

Doctor of Philosophy

The University of Texas at Austin

December 1999

Apparent Horizons in Binary Black Hole Spacetimes

Approved by
Dissertation Committee:

To My Family

Acknowledgments

The binary black hole problem has been and continues to be an exciting challenge and I thank my supervisor, Richard Matzner, for involving me. I also thank him for his careful reading of this dissertation. My thanks to the Center for Relativity for being a fun place to come to work everyday. My warmest appreciation for The Women in Physics Group members who have been my supportive friends. Specifically, I would like to thank Mijan Huq for his everyday help in solving apparent horizons and numerical relativity and for asking me what I want to do with my life at regular intervals, Alex Wurm for his helpful conversations, Luis Lehner for working with me on the binary black hole problem and discussing general relativity, Pablo Laguna for his advice over the years, and Edward Sarnowski for his patient listening. Work in numerical relativity is often a collaborative effort. The success of this thesis is an extension of past successes by others.

Deirdre Marie Shoemaker

The University of Texas at Austin

December 1999

Apparent Horizons in Binary Black Hole Spacetimes

Publication No. _____

Deirdre Marie Shoemaker, Ph.D.

The University of Texas at Austin, 1999

Supervisor: Richard A. Matzner

Over the last decade, advances in computing technology and numerical techniques have lead to the possible theoretical prediction of astrophysically relevant waveforms in numerical simulations. With the building of gravitational wave detectors such as the Laser Interferometric Gravitational-Wave Observatory, we stand at the epoch that will usher in the first experimental study of strong field general relativity.

One candidate source for ground based detection of gravitational waveforms, the orbit and merger of two black holes, is of great interest to the relativity community. The binary black hole problem is the two-body problem in general relativity. It is a stringent dynamical test of the theory. The problem involves the evolution of the Einstein equation, a complex system of non-linear, dynamic, elliptic-hyperbolic equations intractable in closed form. Numerical relativists are now developing the technology to evolve the Einstein equation using numerical simulations. The generation of these numerical

codes is a “theoretical laboratory” designed to study strong field phenomena in general relativity.

This dissertation reports the successful development and application of the first multiple apparent horizon tracker applied to the generic binary black hole problem. I have developed a method that combines a level set of surfaces with a curvature flow method. This method, which I call the level flow method, locates the surfaces of any apparent horizons in the spacetime. The surface location then is used to remove the singularities from the computational domain in the evolution code. I establish the following set of criteria desired in an apparent horizon tracker: (1) The robustness of the tracker due to its lack of dependence on small changes to the initial guess; (2) The generality of the tracker in its applicability to generic spacetimes including multiple black hole spacetimes; and (3) The efficiency of the tracker algorithm in CPU time.

I demonstrate the apparent horizon tracker by evolving a binary black hole spacetime in Kerr-Schild coordinates without the horizon tracking; and then using the information from the horizon tracking to run the simulation further. Because of the apparent horizon tracking, the results shown in this dissertation are of the first binary black hole merger in the Grand Challenge Binary Black Hole Coalescence Alliance code. We have taken a significant step forward in the binary black hole merger problem.

Contents

Acknowledgments	v
Abstract	vi
List of Figures	xi
Chapter 1 Introduction	1
1.1 The Problem: Strong Field Gravitation	1
1.2 The Approach: A Numerical Relativity ToolBox	3
1.3 This Dissertation	7
Chapter 2 The Einstein Equation in Numerical Relativity	9
2.1 The 3+1 Decomposition	11
2.2 Constraint Equations	17
2.3 Equations of Motion	18
2.4 Summary	19
2.5 Other Formulations of General Relativity	20
Chapter 3 Apparent Horizons	22
3.1 Apparent Horizon Definition	22

3.2	Apparent Horizon Equation	26
3.3	Apparent Horizon Excision	30
Chapter 4 Methodology		32
4.1	Algorithms for Finding Apparent Horizons	33
4.2	Level Flow Method	38
Chapter 5 Code Development		45
5.1	The Equation of Motion	45
5.2	Convergence Tests	48
Chapter 6 Apparent Horizon Tracking in Closed-Form Solutions of the Einstein Equation		55
6.1	Schwarzschild Data	56
6.2	Kerr Data	59
6.3	Brill-Lindquist Data	61
Chapter 7 Binary Black Hole Evolutions		70
7.1	Kerr-Schild Metric	71
7.2	Boosted Kerr-Schild Metric	72
7.3	Initial Data	75
7.4	Binary Black Hole Evolution	78
7.5	Black Hole Evolution with Apparent Horizon Tracking	90
7.6	Apparent Horizons in the Binary Black Hole Merger	99
Chapter 8 Conclusions & Future Work		106
8.1	Significance of Results	106
8.2	Near-Future Work	107

Bibliography	110
Vita	117

List of Figures

2.1	The spacetime is foliated into spacelike hypersurfaces.	12
2.2	Sketch of two adjacent hypersurfaces (Σ_t and Σ_{t+dt}).	14
3.1	Penrose and Hawking's collapse of a spherical star leading to the formation of a singularity and trapped surfaces.	24
3.2	The collapse of a spherical star followed by the infall of a thin shell of matter.	25
3.3	Representation of a 2-Sphere embedded in a hypersurface, Σ . .	26
4.1	The level set method embeds the surfaces into an $N + 1$ dimensional surface.	37
4.2	The level set method in theory would find the two apparent horizons by flowing the $N + 1$ -dimensional surface.	38
4.3	The level flow method uses a set of surfaces.	41
4.4	Plot of five levels ($\kappa = 0.14, 0.12, 0.10, 0.08, 0.06$) of constant divergence of outgoing null geodesics.	42
4.5	Representation of the decision making process for multiple surfaces in the level flow method	44
5.1	The Crank-Nicholson scheme molecule	46

5.2	The two functions used as speed functions in the level set method.	49
5.3	The function $f(x)$ is zoomed in on region of interest.	50
5.4	The convergence factor for ψ os Schwarzschild data	52
5.5	The convergence factor for κ os Schwarzschild data	53
5.6	Convergence factor for ψ of Brill-Lindquist data	54
6.1	Apparent horizons for the Schwarzschild metric for 17^2 .	58
6.2	Apparent horizon for 33^2 .	59
6.3	The apparent horizons for the Kerr metric	60
6.4	The apparent horizon for Brill-Lindquist data at critical separation	62
6.5	Brill-Lindquist data at a separation $1.5M$	63
6.6	The absolute value of the maximum of κ per iteration	64
6.7	The starting surface of the level flow method for a separation of $d=2.0M$	65
6.8	Level set for $d=2.0M$	66
6.9	The single surface is about to fission into two surfaces.	66
6.10	The absolute value of the maximum of expansion, κ , per iteration	67
6.11	The points can “bunch” on the surface during flow causing the finite difference scheme to fail.	67
6.12	The flow of the surfaces in Brill-Lindquist data	68
6.13	The flow of the surface in Brill-Lindquist data plotted together.	69
7.1	The shift and lapse for Eddington-Finkelstein data	74
7.2	Initial data for the binary black hole merger run	79
7.3	The lapse and shift for two Eddington-Finkelstein holes	81
7.4	g_{xx} sliced at $x = z = 0$ versus time	85

7.5	g_{xx} sliced at $y = z = 0$ versus time	86
7.6	$HC/ HC $ sliced at $x = z = 0$ versus time	86
7.7	$HC/ HC $ sliced at $y = z = 0$ versus time	87
7.8	Snapshots of g_{xx} at $z = 0$	88
7.9	Snapshots of $HC/ HC $ at $z = 0$	89
7.10	g_{xx} sliced at $x = z = 0$ versus time from $0M$ to $8M$	92
7.11	g_{xx} sliced at $y = z = 0$ versus time from $0M$ to $8M$	93
7.12	$HC/ HC $ sliced at $x = z = 0$ versus time from $0M$ to $8M$	94
7.13	$HC/ HC $ sliced at $y = z = 0$ versus time from $0M$ to $8M$	94
7.14	Snapshots of g_{xx} sliced at $z = 0$	95
7.15	Snapshots of $HC/ HC $ sliced at $z = 0$	96
7.16	Snapshots of g_{xx} sliced at $z = 0$	97
7.17	Snapshots of $HC/ HC $ sliced at $z = 0$	98
7.18	Snapshots of the apparent horizon(s) with the masks included.	100
7.19	A plot of the apparent horizons for the merged binary black hole.	101
7.20	A plot of the apparent horizons after the black holes have merged.	102
7.21	The apparent horizons are plotted in each plane on top of each other to illustrate the deformation of the horizons.	103
7.22	The numerically computed area of the apparent horizon versus time for the binary black hole grazing collision.	105

Chapter 1

Introduction

1.1 The Problem: Strong Field Gravitation

The desire to study strong field general relativity has led to the investigation of one of the most compelling problems in numerical relativity today: the simulation of the multiple-black-hole spacetime. Binary black hole interactions are believed to occur in the universe within approximately $300Mpc$ at a rate of about one per year as a conservative estimate [42,61]. Despite the infrequency of events involving black holes, they remain one of the most likely events to be detected by ground based gravitational wave detectors.

The reason for the likelihood of detection of waveforms resulting from black hole collisions lies in the weakness of the gravitational field. In the weak gravitational limit, the expression for the power carried away in quadrupole radiation is

$$L = \left\langle \frac{1}{5} \frac{G}{c^5} \frac{d^3 Q_{ij}}{dt^3} \frac{d^3 Q^{ij}}{dt^3} \right\rangle, \quad (1.1)$$

where $\langle \rangle$ indicates an average over several periods of the radiation. In a

closed, radiating system with a time scale for motions within the sources, $T \approx r^3/M$, the total radiated power has been estimated by L.S. Finn [26] as:

$$L \propto \left(\frac{c^5}{G}\right)^{-1} \left(\frac{MR^2}{T^3}\right)^2. \quad (1.2)$$

However, he points out that generally this is an optimistic estimate of the power radiated, because it assumes maximal contribution from the moving mass to the quadrupole radiation. In addition, eqn. (1.2) is a luminosity-squared $\left(\frac{MR^2}{T^3}\right)$ divided by a “fundamental power.” Since the fundamental power:

$$\frac{c^5}{G} = 3.6 \times 10^{59} \text{ erg/s} \quad (1.3)$$

is so large, the actual emitted gravitational radiation-power is small unless R and T are both close to 1 when expressed in geometricized units in which $M = 1$. The power radiated is small unless we deal with very compact objects such as neutron stars or black holes.

Such a dimensional analysis gives a physical insight into the weakness of the gravitational interaction and the weakness of sources that do not involve compact objects. The signal of gravitational interaction occurring far from us, the observers, will manifest itself as tiny ripples in our geometry. The most violent, plausibly frequent interactions, collisions involving black holes or neutron stars, are expected to be rare and will occur very far away from us. Typically, distant events will only affect our local spacetime in fluctuations on the order of 10^{-21} units of strain on the detector. Detectors sensitive to this scale must be built to obtain information about these distant sources. For this observed information to be useful, theoretical models of the observable interactions must be devised.

The physical signature of gravitational fields associated with compact objects is the gravitational waveform. Obtaining a database of gravitational waveforms involves solving the Einstein equation, which is a highly non-linear, coupled elliptic-hyperbolic set of partial differential equations. These partial differential equations are intractable with closed form methods. Numerical methods, even though they are highly difficult to implement, are the only and best means available to study generic, strong field, gravitational interactions.

Over the last decade, numerical and technical advances have created the possibility of numerically solving the Einstein equation for dynamic systems and detecting gravitational radiation emitted from astrophysical sources. Experimental apparatus capable of detecting gravitational waves from compact objects in the universe is under construction (such as the Laser Interferometric Gravitational-wave Observatory in the United States). The detectors represent the possibility of verifying (or falsifying) the predictions of gravitational radiation produced by theoretical models.

1.2 The Approach: A Numerical Relativity ToolBox

Members of the numerical relativity community are building the tools necessary to describe a series of very complicated spacetimes to facilitate the study of scenarios involving strong field general relativity. Such scenarios include neutron star and black hole collisions, supernovae, and extragalactic nuclei. Binary black hole interactions are expected to be within the range of early generations of ground based gravitational wave detectors. To predict the

waveforms generated by dynamic black hole spacetimes, numerical codes are being constructed.

The goal is to develop a single, *generic*, numerical code that will, given an initial data set, evolve the resulting spacetime by a set of rules called the Einstein equation. The Einstein equation is written as a Cauchy problem by introducing a sequence of 3-spaces evolving in time. The code I use in this dissertation implements a 3+1 formulation similar to the Arnowitt, Deser, and Misner [6] approach. The code is being built from a toolbox containing tools from many collaborators flexible enough to be useful in a variety of possible situations. A very large amount of this work resulted from the National Science Foundation’s Binary Black Hole Grand Challenge Alliance [7]. The final code will be used for single and binary black hole mergers with various orbits, speeds, and spins of the black holes. In the end, the code will be designed to act as a “theoretical laboratory” for the study of general relativity.

Building a code capable of reproducing the dynamics of a binary black hole collision, including the orbit, inspiral, merger, and ringdown phases [27], is an arduous process. It is a process that has been on-going for the past several years and continues today. There are three parameters that characterize black holes: mass, M , angular momentum a , and charge, Q . Astrophysical black holes are assured to have a very small charge, so our simulation always have $Q = 0$. Evolving a black hole involves the following:

- Initial Data
- Finite Differencing of the Equation of Motion
- Singularity Excision

- Outer Boundaries
- Wave Extraction.

The items will be addressed in detail later in the text. For now, let me briefly examine each one.

The Einstein equation will be reformulated into a 3+1 form as mentioned previously. This form is an initial value problem called a Cauchy problem separating space and time and making the dynamics manifest. A set of initial data on the space at the initial time must be specified. The Einstein equation in 3+1 form now has evolution equations, or equations of motion, that we discretize on the computational grid. The derivatives are taken care of by finite difference molecules that are second order accurate in space. (Other discretization techniques may be used.) The difficulties with the finite differencing arise when we excise the region of the grid containing the singularity. We cannot compute through a singularity due to the huge gradients in the grid functions. Unruh [58] suggested excising the black hole at its apparent horizon (the topic of this dissertation). The resulting “hole” in the grid we call a mask since it hides the singularity from view. Finding the correct finite difference molecules for points on the boundary of the masked region is difficult. The centered differencing used everywhere else in the grid cannot be used here. Causal differencing [39] is a physically motivated method to handle superluminal shift vectors, such as occur at the mask boundaries when we do apparent horizon excision. The difficulty of correctly implementing causal differencing increases as dynamics are added to the problem.

There is a separate set of problems associated with the outer domain of our simulations. We cannot locate the outer boundaries of space at null infinity

as we do in nature; therefore, unphysical boundary conditions are required at finite radii. Due to the limits in computer memory, the boundaries of the grid tend to be too close to the black hole. Here “too close” means the errors at the boundary of the computation are unacceptably large. This leads to increasing interior errors as errors in the boundary propagate into the interior.

Wave extraction is necessary to obtain the gravitational waveforms from the simulation. Future simulations will generate waveforms for comparison with experiment (such as LIGO). Wave extraction is not demonstrated in this dissertation, but will be part of the future work.

There have been fully 3-dimensional simulations of long term single black holes (including Kerr spinning holes), in the Grand Challenge Alliance codes [31, 22]. The next step in building a code capable of simulating astrophysically relevant scenarios was a moving black hole. The difficulties in determining good finite difference molecules increase since previously masked points are uncovered. However, moving black holes have been evolved successfully [38,22].

We are interested in the case of two black holes in a grazing collision, the precursor to orbiting black holes. We use all the 3-dimensional tools built for isolated stationary and moving black holes to evolve a grazing collision of spinning black holes. The role of this dissertation is to locate the apparent horizons used to mask the singularity region, and to demonstrate the utility of this procedure in carrying out a dynamical evolution.

Recent progress has led to apparent horizon tracking algorithms capable of locating single, generic, apparent horizons [46,2,38,59,33]; however, this dissertation will describe the first algorithm capable of detecting *multiple* apparent horizons in a generic spacetime with the following criteria:

- (1) The robustness of the tracker due to its lack of dependence on small changes to the initial guess;
- (2) The generality of the tracker in its applicability to generic spacetimes including multiple back hole spacetimes; and
- (3) The efficiency of the tracker algorithm in CPU time.

This will aid in the evolution of *binary* black hole evolutions. The algorithm is called the level flow method. It is based on a curvature flow method [60] for robustness combined with a level set of surfaces which furnishes a coordination to provide the signal for possible topology change (one surface to two) in the flow to the apparent horizon.

1.3 This Dissertation ...

This dissertation is divided into eight chapters. Chapter 2 presents the Einstein equation and its formulation as an initial value problem. The resulting evolution equations and constraints are listed. Chapter 3 is dedicated to defining apparent horizons and the apparent horizon equation. The use of the apparent horizon as an excision “no-boundary” is also discussed.

A large portion of the work behind this dissertation is the development of the level flow method to locate apparent horizons, presented in Chapter 4. I discuss the methods used by others to locate apparent horizons as well as my method including in each case the successes and deficiencies. The code that implements the level flow method is detailed in Chapter 5 including tests to verify the accuracy of the finite differencing.

In Chapter 6 I demonstrate the “correctness” of the level flow method through a series of closed-form tests. I use Schwarzschild, Kerr, and Brill-Lindquist closed-form solutions to test the code and to explicate the method of apparent horizon location.

In Chapter 7, I report, with excitement, our success in using the apparent horizon tracker to run a binary black hole collision to merger. I present the specific case of a short grazing binary black hole merger in Kerr-Schild coordinates with each (equal) mass hole having a spin of $0.5M\hat{z}$ and velocity of $0.5c\hat{x}$ and $-0.5c\hat{x}$. I ran the Grand Challenge Alliance code [39] with an excision scheme to remove the singularities based on predictions of the apparent horizon location. Because of the horizon tracking, we are able for the first time, to obtain an evolution through to merger in the Alliance code. We are currently working to improve the evolution enough to extract waveforms.

Finally, the last chapter summarizes the thesis work discussing the successes and deficiencies. Current and future work is presented. Ideas of improving the apparent horizon tracker are also discussed. The binary black hole collision is not solved yet, but a significant step forward has been taken.

Chapter 2

The Einstein Equation in Numerical Relativity

General relativity is a theory of the pseudo-Riemannian geometry of spacetime. In this description, gravitational fields emitted from a source behave like waves rippling the spacetime. Near the source the waves distort the spacetime geometry greatly, but far away from the source the spacetime is asymptotically flat, meaning the spacetime is approximated by a Minkowski spacetime. The spacetime is a continuous four dimensional manifold \mathcal{M} on which the metric g_{ab} with signature $(-+++)$ is defined. The notion that geometry is related to matter and energy is mathematically given by the Einstein equation:

$$G_{ab} = 8\pi T_{ab}, \tag{2.1}$$

following Wald's notation [62] where G_{ab} is the Einstein tensor, T_{ab} is the stress energy tensor for non-gravitational sources, and 8π is the constant in units G (gravitational constant) = c (speed of light) = 1. In the end of this discussion, we will limit ourselves to vacuum spacetimes, $G_{ab} = 0$, appropriate to the

study of spacetimes containing black holes.

In numerical relativity we wish to manifestly express the dynamics of the Einstein equation. Following the theorem by Wald [62], if the spacetime (\mathcal{M}, g_{ab}) is globally hyperbolic with a spacelike Cauchy surface Σ (which together means that the domain of dependence of Σ is the entire manifold, \mathcal{M}); and if we consider what is known as a linear, diagonal second order hyperbolic system on it which consists of n linear equations for n unknown functions, $\phi_1 \dots \phi_n$ of the form

$$\gamma^{ab}\nabla_a\nabla_b\phi_i + \sum_j (A_{ij})^a\nabla_a\phi_j + \sum_j B_{ij}\phi_j + C_i = 0 \quad (2.2)$$

(γ^{ab} , $(A_{ij})^a$, B_{ij} , C_i independent of ϕ_l) constructable on it, then eqn. (2.2) has a well-posed initial value formulation on Σ . In this context, “well-posed” means that the solution and its derivatives depend continuously on the data and its derivatives are the initial surface. Eqn. (2.2) does not describe the Einstein equation for two reasons: a) the Einstein equation is a constrained hyperbolic system; b) the Einstein equation is quasi-linear, meaning the coefficients actually depend on the variable ϕ_i . This second point is treated by an immediate extension, which generates at least local well posedness for the Einstein system.

Among other things, point a) means that the Einstein equation only involves six evolution equations since in this formulation four of the equations, the constraint equations, involve no time derivatives. Thus the Einstein system is underdetermined for the full set of ten components of the metric, using terminology due to Wald [62,p.260]. This aspect of point a) is treated by Wald (building on extensive literature) by introducing harmonic coordinates [62]. This reduces the number of variables to be evolved to six, the same as the

number of equations in the Einstein system. Other viewpoints hold that the Einstein equations are overdetermined because there are twelve algebraically independent evolution equations plus four constraint equations determining only twelve independent variables. In either circumstance, the Einstein space-time is well posed in terms of data that solves the constraint equations on the hypersurface Σ .

This dissertation does not use harmonic coordinates; we leave the coordinate specification entirely free, in terms of the lapse function and shift vector defined in section 2.1. Choice of lapse and shift has the effect of reducing the evolved system to the required size in the same way that the harmonic coordinates do. There has recently been a resurgence of interest in the question of in which forms the Einstein system is explicitly well posed. We do not pursue this question further, but we refer the reader to the recent literature [3,28].

The spacetime is sliced into a sequence of Cauchy hypersurfaces, Σ_τ , parameterized by time τ , a scalar function of the spacetime. In this manner the Einstein equation becomes a set of ten partial differential equations with two dynamic variables, γ_{ab} and K_{ab} . γ_{ab} is the three-space metric and K_{ab} is the extrinsic curvature describing the curvature of Σ_τ relative to the embedding spacetime. Note that we will use γ_{ab} as the spatial metric and g_{ab} as the spacetime metric. The idea of foliating the spacetime is illustrated for a three-dimensional spacetime in fig. (2.1).

2.1 The 3+1 Decomposition

The procedure for decomposing the spacetime into space+time (3+1) was performed by Arnowitt, Deser, and Misner and is well documented [63, 21];

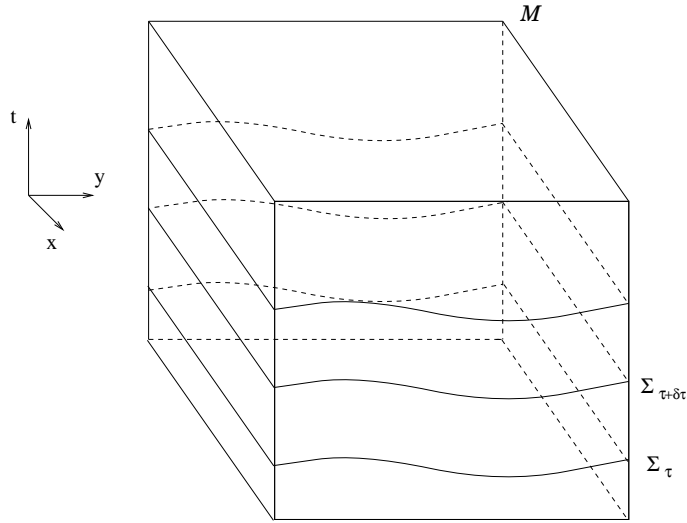


Figure 2.1: Sketch of the foliation of a 3-dimensional spacetime manifold \mathcal{M} into spacelike hypersurfaces, Σ_τ , sliced in time.

therefore, we will limit the discussion to a review of the equations and variables. The nature of a Cauchy procedure is an initial value problem in which quantities on an initial slice (i.e. at an initial time) must be appropriately specified. Once the initial slice's quantities are specified, the Einstein equation determines the values of these quantities on the past and future slices.

Fig. (2.2) and the 3+1 metric

$$ds^2 = -\alpha^2 dt^2 + \gamma_{ij}(dx^i + \beta^i dt)(dx^j + \beta^j dt). \quad (2.3)$$

are used for the following definitions. The foliation is characterized by a closed one-form, $\Omega_a \equiv \nabla_a \tau$. The choice of slicing is contained in the lapse function, α , defined as

$$\alpha^{-2} \equiv -g^{ab} \nabla_a \tau \nabla_b \tau. \quad (2.4)$$

The timelike, unit normal to the spacelike hypersurfaces, Σ_τ , is

$$n_a = -\alpha \nabla_a \tau. \quad (2.5)$$

A timelike vector tangent to the world line of a coordinate observer, t^a , is constructed such that

$$t^a = \alpha n^a + \beta^a, \quad (2.6)$$

and defines a spacelike vector describing the shift in the spatial coordinates between adjacent hypersurfaces, β^a , such that

$$\beta^a n_a = 0. \quad (2.7)$$

An observer will measure the elapsed proper time between hypersurfaces Σ_τ and $\Sigma_{\tau+\delta\tau}$ along the normal from point P to point Q as αdt . The coordinate time and proper time will often differ, and the observer moving along the coordinate, x^i , actually travels from point P to point R . The difference in spatial coordinates Q and R on $\Sigma_{\tau+d\tau}$ is related to the shift vector by $\beta^i dt$. Specifying the lapse function and shift vector of the slicing is equivalent to choosing the coordinate labeling of the spacetime.

Before writing down the Einstein equation in the 3+1 formalism a few concepts need to be defined. A projection tensor, \perp^a_b , is introduced to define the spatial parts of tensors:

$$\perp^a_b \equiv \delta^a_b + n^a n_b. \quad (2.8)$$

The notation \perp applies the projection tensor to every free index. The spatial metric is defined as

$$\gamma_{ab} = g_{ab} + n_a n_b. \quad (2.9)$$

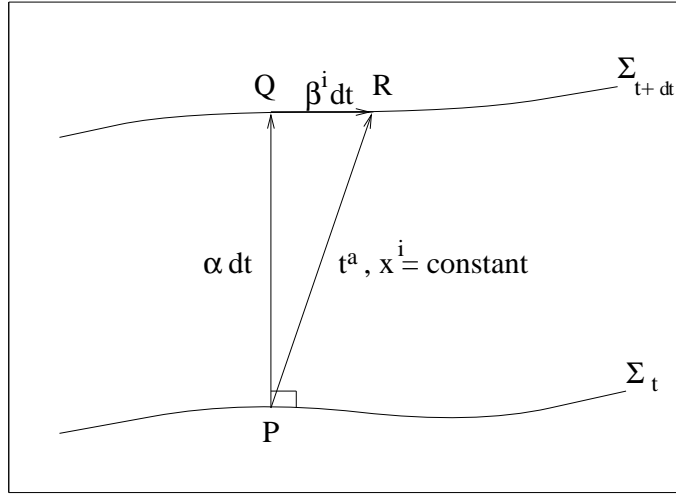


Figure 2.2: Sketch of two adjacent hypersurfaces (Σ_t and Σ_{t+dt}).

The derivative operator, D_a , will be used here and in future chapters,

$$D_a \equiv \perp \nabla_a. \quad (2.10)$$

D_a is a natural derivative operator for operations on spatial tensors due to its compatibility with the spatial metric:

$$D_a \gamma_{ab} = 0. \quad (2.11)$$

(A spatial tensor is one for which $\perp T^{a\dots} = T^{a\dots}$). D_a acts on purely spatial tensors in the following manner:

$$D_a T^{b_1\dots b_l}_{c_1\dots c_m} = \perp^{b_1}_{d_1} \dots \perp^{b_l}_{d_l} \perp^{e_1}_{c_1} \dots \perp^{e_m}_{c_m} \perp^f_a \nabla_f T^{d_1\dots d_l}_{e_1\dots e_m}. \quad (2.12)$$

The last tool required to write down the Einstein equation in 3+1 form compares tensors at different points, p and $p+\Delta p$. In a curved spacetime, there is no sensible notion of parallelism. To compare tensors at different points it is helpful to define the notion of Lie dragging the tensor at $p + \Delta p$ back to p

and subtracting this new tensor from the original one to get a difference. This difference is called a Lie difference [53]. The basic concept of Lie dragging is that of an infinitesimal motion of the points of the space along the vector field defined at each point. Since a second infinitesimal vector can be thought of as connecting two adjacent points, the Lie dragged vector is the vector connecting the points; a definition for tensors can be built up similarly. The Lie derivative with respect to a vector field, v^a , is defined by:

$$\mathcal{L}_v T^{a_1 \dots a_k}_{b_1 \dots b_l} = \lim_{\Delta p \rightarrow 0} \frac{\phi_p^* T^{a_1 \dots a_k}_{b_1 \dots b_l} - T^{a_1 \dots a_k}_{b_1 \dots b_l}}{\Delta p}, \quad (2.13)$$

with all tensors evaluated at p [62]. $T^{a_1 \dots a_k}_{b_1 \dots b_l}$ is a smooth tensor field and $\phi_p^* T^{a_1 \dots a_k}_{b_1 \dots b_l}$ is the result of Lie dragging the tensor from $p + \Delta p$ to p . For a scalar function, f , the Lie derivative is

$$\lim_{\Delta p \rightarrow 0} \frac{f^*(p_0) - f(p_0)}{\Delta p} = \lim_{\Delta p \rightarrow 0} \frac{f(p_0 + \Delta p) - f(p_0)}{\Delta p} = \left[\frac{df}{dp} \right]_{p_0} \quad (2.14)$$

where $f^*(p_0) = f(p + \Delta p)$ is the value of the scalar dragged back to p_0 . For a scalar function, the Lie derivative is the same as the ordinary notion of a derivative.

The curvature of the slices, Σ_τ , embedded in the spacetime is described by the extrinsic curvature tensor, which is determined by the gradients of the timelike normals to Σ_τ . The equation for the extrinsic curvature of a t =constant surface Σ_t is

$$K_{ab} = - \perp \nabla_{(a} n_{b)}. \quad (2.15)$$

Expressing the decomposition of the derivative of the normal fields into a hypersurface-tangential piece (K_{ab}) and a hypersurface-orthogonal piece leads to:

$$\nabla_a n_b = -K_{ab} - n_a a_b, \quad (2.16)$$

where the 4-acceleration is $a^b = n^a \nabla_a n^b$. Using eqn. (2.15) and eqn. (2.16), K_{ab} is expressed in the form:

$$K_{ab} = -\frac{1}{2} \perp \mathcal{L}_n g_{ab} = -\frac{1}{2} \mathcal{L}_n \gamma_{ab}. \quad (2.17)$$

The following two equations are needed to derive eqn. (2.17):

$$\mathcal{L}_n g_{ab} = n^c \nabla_c g_{ab} + g_{cb} \nabla_a n^c + g_{ac} \nabla_b n^c = \nabla_a n_b + \nabla_b n_a = 2\nabla_{(a} n_{b)} \quad (2.18)$$

and

$$\mathcal{L}_n \gamma_{ab} = n^c \nabla_c \gamma_{ab} + \gamma_{cb} \nabla_a n^c + \gamma_{ac} \nabla_b n^c = 2(\nabla_{(a} n_{b)} + n_{(a} a_{b)}) = -2K_{ab}. \quad (2.19)$$

Eqn. (2.17) is determined by first noting eqn. (2.18) where the first equality in eqn. (2.18) is a standard way to express the Lie derivative in terms of the covariant derivative; in fact the covariant derivatives could be replaced by ordinary derivatives in the first form (the connections cancel). However, the given form allows us to use the covariance of g_{ab} to drop it from the equation.

The second equality in eqn. (2.17) holds by noting that

$$g_{ab} = \gamma_{ab} - n_a n_b, \quad (2.20)$$

and thus $\mathcal{L}_n g_{ab}$ computed according to eqn. (2.18) equals $\mathcal{L}_n \gamma_{ab} - 2n_{(a} a_{b)}$; the term involving the acceleration is removed from eqn. (2.17) by the projection operator \perp .

The intrinsic curvature of the hypersurface is given by another tensor, the spatial Riemann tensor, \mathcal{R}_{abc}^d , and may be defined via the action of D_a on an arbitrary spatial dual vector, W_a :

$$(D_a D_b - D_b D_a) W_c = \mathcal{R}_{abc}^d W_d. \quad (2.21)$$

The spatial Ricci tensor, \mathcal{R}_{ab} , and the spatial Ricci scalar, \mathcal{R} , are constructed:

$$\mathcal{R}_{ab} = \mathcal{R}_{acb}{}^c \quad (2.22)$$

$$\mathcal{R} = \mathcal{R}_a{}^a, \quad (2.23)$$

where the indices are raised and lowered using the spatial metric, γ_{ab} , and its inverse, γ^{ab} . The following matter terms are measured by observers moving orthogonally to the slices and are defined as the local energy density (ρ), the momentum density (j^a), and the spatial stress energy tensor (S_{ab}):

$$\rho = T_{ab}n^an^b \quad (2.24)$$

$$j^a = -\perp(T^{ab}n_b) \quad (2.25)$$

$$S_{ab} = T_{ab} \quad (2.26)$$

The trace of the spatial stress energy tensor is $S = T^a{}_a$.

2.2 Constraint Equations

The decomposition in the 3+1 form begins with the derivation of the constraint equations. We do not give the full derivation here but note that these equations are derived using Gauss-Codazzi equations [62] and the following 3+1 decomposition rule [21] for any generic symmetric tensor of dimensional type (0,2):

$$\sigma_{ab} = \perp \sigma_{ab} - 2n_{(a} \perp \sigma_{b)\hat{n}} + n_an_b\sigma_{\hat{n}\hat{n}}; \quad (2.27)$$

where \hat{n} denotes a contraction with n^a , such as $W_{\hat{n}} \equiv W_a n^a$. The decomposition leads to constraint and evolution equations. The constraint equations must be satisfied by the geometric and matter variables on every hypersurface.

The first constraint is called the *Hamiltonian constraint*:

$$\mathcal{R} + K^2 - K^a_b K^b_a = 16\pi\rho, \quad (2.28)$$

where K is the trace of the extrinsic curvature

$$K \equiv K^a_a. \quad (2.29)$$

The second constraint equation is called the *momentum constraint*:

$$D_b K^{ab} - D^a K = 8\pi j^a. \quad (2.30)$$

Note that equations (2.29) and (2.30) involve only spatial tensors, not time derivatives of spatial tensors explicitly. They are constraint equations and must be satisfied by the 3+1 variables γ_{ab} and K_{ab} on every slice (at all times).

2.3 Equations of Motion

The first set of evolution equations for the dynamic 3+1 variable, γ_{ab} , follows from eqn. (2.17) using Lie-differentiation along the vector field

$$t^a = \alpha n^a + \beta^a \quad (2.31)$$

as the time derivative. The equation is written:

$$\mathcal{L}_t \gamma_{ab} = -2\alpha K_{ab} + \mathcal{L}_\beta \gamma_{ab}. \quad (2.32)$$

The second evolution equation for the dynamic 3+1 variable K_{ab} is derivable from the Einstein equation and the decomposition procedure for a symmetric tensor eqn.(2.27):

$$\mathcal{L}_t K^a_b = \mathcal{L}_\beta K^a_b - D^a D_b \alpha + \alpha(\mathcal{R}^a_b + K K^a_b + 8\pi(\frac{1}{2}\perp^a_b(S - \rho) - S^a_b)). \quad (2.33)$$

The equations can be expressed in terms of a coordinate basis. The Hamiltonian and momentum constraints are respectively:

$$K^2 - K_{ij}K^{ij} + R = 16\pi\rho_0 \quad (2.34)$$

$$D_i(K^{ij} - \gamma^{ij}K) = 8\pi j^i \quad (2.35)$$

The evolution equations for the dynamical variables γ_{ij} and K_{ij} are:

$$\partial_t \gamma_{ij} = -2\alpha K_{ij} + \mathcal{L}_\beta \gamma_{ij} \quad (2.36)$$

$$\partial_t K_{ij} = -D_i D_j \alpha + \alpha [R_{ij} + K K_{ij} - 2K_{il} K_j^l] - \alpha [S_{ij} - \frac{1}{2} \gamma_{ij} (S - \rho)] + \mathcal{L}_\beta K_{ij}, \quad (2.37)$$

where

$$\mathcal{L}_\beta \gamma_{ij} = \beta^k \partial_k \gamma_{ij} + \gamma_{kj} \partial_i \beta^k + \gamma_{ik} \partial_j \beta^k \quad (2.38)$$

$$\mathcal{L}_\beta K_{ij} = \beta^k \partial_k K_{ij} + K_{kj} \partial_i \beta^k + K_{ik} \partial_j \beta^k. \quad (2.39)$$

2.4 Summary

In this dissertation, I use vacuum spacetimes only. The 3+1 equations in vacuum can be summarized as follows. The constraint equations in vacuum are:

$$\mathcal{R} + K^2 - K^a{}_b K^b{}_a = 0 \quad (2.40)$$

$$D_b K^{ab} - D^a K = 0, \quad (2.41)$$

and the evolution equations in vacuum are:

$$\partial_t \gamma_{ij} = -2\alpha K_{ij} + \mathcal{L}_\beta \gamma_{ij}, \text{ and} \quad (2.42)$$

$$\partial_t K_{ij} = -D_i D_j \alpha + \alpha [R_{ij} + K K_{ij} - 2K_{il} K_j^l] + \mathcal{L}_\beta K_{ij}. \quad (2.43)$$

The solution of the 3+1 form of the Einstein equation is found in two steps. First, the initial data are specified by choosing a coordinate system, choosing data K_{ab} and γ_{ab} on the initial slice, and choosing the initial slice topology. Due to the elliptic nature (second derivatives of the metric appear in the 3-curvature, \mathcal{R}) of the constraint equations, this is a complicated procedure. One approach is presented by York [63]. We will return to the question of initial data in Chapter 7. The second step is the evolution. This involves choosing α and β_i everywhere, which is the same as imposing the coordinate conditions that are left free due to the covariant nature of the Einstein equation. In such a way the spacetime is generated slice by slice. The spacetime is evolved using only the evolution equations using the constraints as a check. The evolution equations preserve the constraints in theory, and also do so numerically as long as the finite differencing of the equations is done carefully [19]. In practice, problems inevitably arise and the computational evolution ends.

2.5 Other Formulations of General Relativity

Although here we will be applying the apparent horizon locator to a spacetime computed using the 3+1 form of the Einstein equation, the apparent horizon locator is also applicable to spacetimes generated by other formalisms of the Einstein equation. There are three different approaches of decomposition available to achieve a form that allows stepwise evolution. The approaches depend on the slicing of the spacetime into space and time. The three approaches are 1) evolution of spacelike 3-surfaces in time [6], 2) evolution of character-

istic 3-surfaces in time [10], and 3) evolution of hyperbolic 3-surfaces in time [35,36].

We have already discussed the first approach, decomposing the spacetime into spacelike hypersurfaces foliating the spacetime in a time sequence. The second approach, the characteristic approach, was pioneered by Bondi, van der Berg, Metzner [13], Sachs [52], and Penrose [49]. The spacetime is sliced into null hypersurfaces of constant advanced or retarded time. This method allows for compactification of infinity, allowing computations to reach infinity in a finite amount of effort. Unfortunately, the construction of a coordinate system near a pair of black holes is difficult in the characteristic method, and currently unsolved in general. The third approach slices the spacetime into spacelike hyperboloidal surfaces that become null at infinity. This method also can compactify infinity. However, this method is undeveloped in 3-dimensional, numerical situations due to the large number of variables introduced in the hyperbolic formalism. In any case, the level flow method of tracking apparent horizons is applicable.

Chapter 3

Apparent Horizons

My goal is to locate apparent horizons; therefore, it is very important to understand the properties of an apparent horizon and its mathematical definition. In this chapter, I define the apparent horizon in a physical sense and in a mathematical sense. The role of apparent horizons in the evolution code is also discussed.

3.1 Apparent Horizon Definition

Observational evidence such as gravitational lensing has shown that light is deflected by the gravitational field of massive objects. In fact, an object with significant enough weight will collapse under its own mass, creating a black hole with a gravitational pull so strong that light is deflected to the degree that it cannot escape from the object. (The massive object warps the spacetime. The light is traveling in the straightest path, a geodesic, but that straightest path exists in a curved spacetime.) The strongest such case occurs when a star collapses into a black hole. In that case the curvature eventually becomes sin-

gular at events within the black hole's horizon. Because of the nonlinearity of the Einstein equation, even pure vacuum black holes (which are called eternal black holes because they did not form from collapse but existed in the distant past) can exist with no matter present; these still contain singularities.

To quantify the idea of deflection, consider a thought experiment introduced by Penrose [34]. A wavefront of light is emitted by a flashing light source at the center of a spherical distribution of matter where the matter is assumed transparent. In weak gravitational situations, matter will deflect the light negligibly and the light will diverge, spreading out to radiative infinity, (\mathcal{J}^+). However if the matter has a strong gravitational field, the light converges and never reaches \mathcal{J}^+ . An outgoing wavefront that is defined by converging outgoing null rays is called a *trapped surface*. A boundary exists between the spherical wavefronts with positive convergence and those with negative convergence. Such a surface is called a *marginally trapped surface*.

There are two surfaces of special interest to the study of black holes: the event horizon and the apparent horizon. The *event horizon* is the boundary between light rays that will and will not reach \mathcal{J}^+ ; therefore, it is the boundary between what an observer at infinity will be able to detect and not be able to detect. By its definition, the event horizon is global in nature, meaning the entire spacetime must be known to determine its location. In contrast, an *apparent horizon* is defined locally, meaning it is a 2-surface defined at a particular instant in time. The apparent horizon is always the outermost marginally trapped surface in a spacelike hypersurface at each instant of time. The definition of the apparent horizon means it can exhibit discontinuous movement through time. In contrast, an event horizon can only exhibit continuous movement as a function of time.

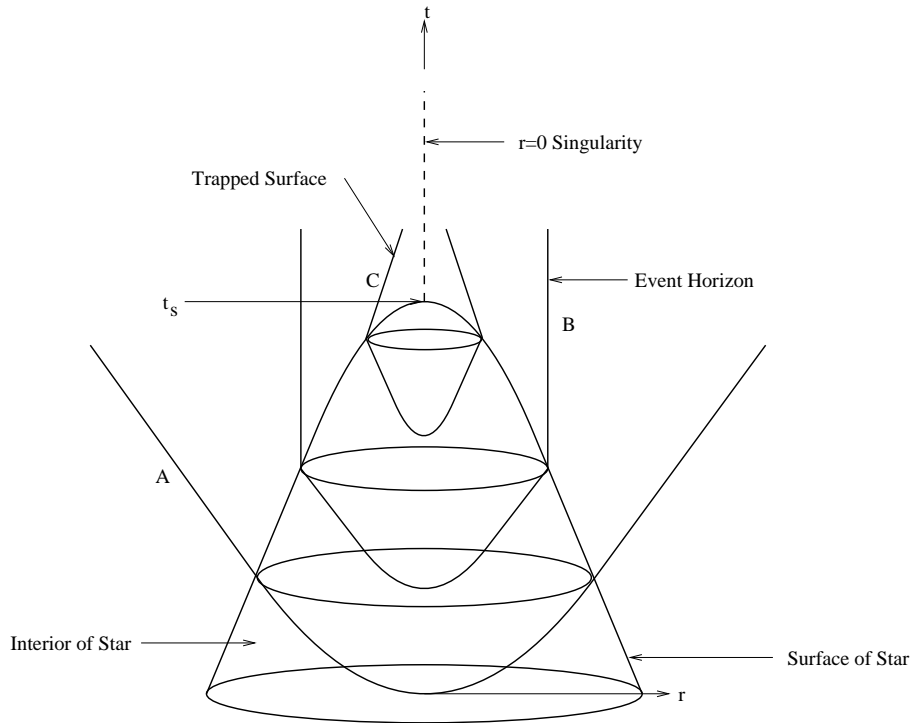


Figure 3.1: Penrose and Hawking’s collapse of a spherical star leading to the formation of a singularity and trapped surfaces.

To illustrate this effect, consider the example of a spherically collapsing massive star as described by Hawking and Penrose [34]. Fig. (3.1) depicts the spherical collapse of a star. The star forms a singularity at $r = 0$ beginning at some time, t_s . Imagine that spherical wavefronts of light are emitted by the star as it collapses. A wavefront, A , escapes the collapsing star’s gravitational pull at the time $t_A < t_s$, and reaches the observer at \mathcal{J}^+ . A later wavefront, B ($t_A < t_B < t_s$), does not escape to the observer at infinity but neither does it converge onto the singularity. This is a marginally trapped surface and the apparent horizon. If no additional matter falls onto the star, this surface is the event horizon. A spherical wavefront emitted even later during the collapse,

C ($t_B < t_C < t_s$), converges towards the singularity, thus describing a loci of trapped surfaces. In this example, the apparent and event horizons coincide.

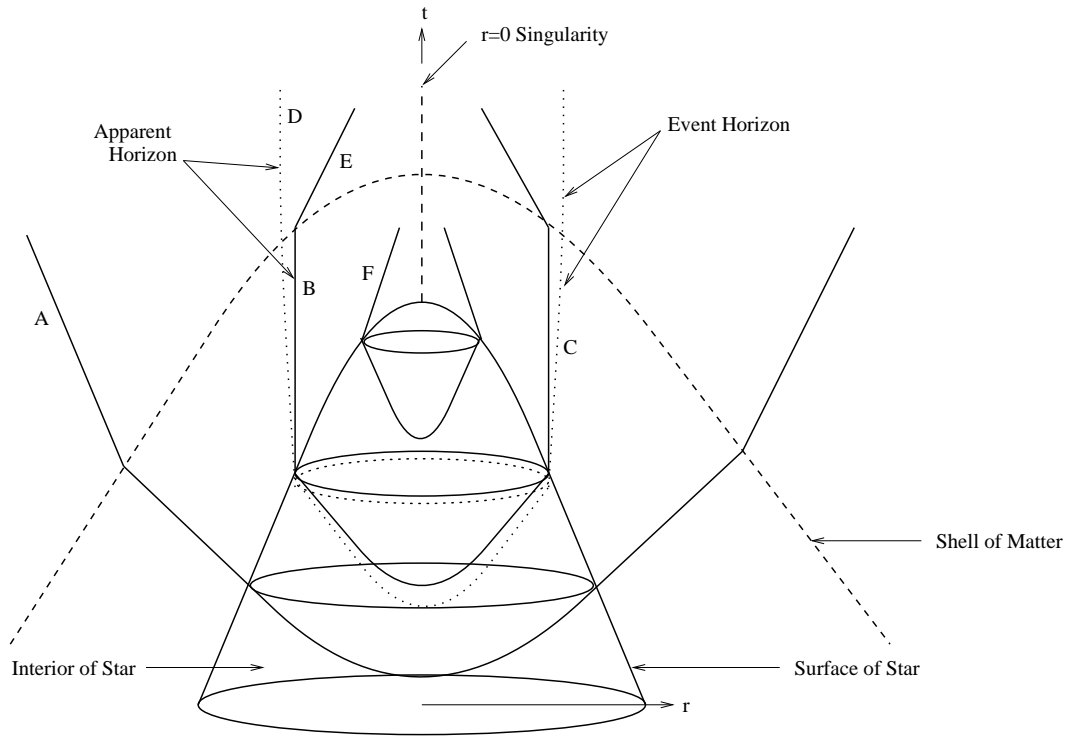


Figure 3.2: The collapse of a star followed by the collapse of a spherical shell of matter, dashed line, onto the star. The apparent horizon appears, B , and then moves discontinuously out to D as the thin shell of matter passes. The event horizon is the continuous surface labeled C and D and drawn with a dotted line.

Considering a more complicated example illustrates the difference between the apparent horizon and the event horizon. Once again imagine a star undergoing spherical collapse but now with a thin shell of matter collapsing onto the star at a later time. A spherical wavefront of light, A , is emitted by the star and escapes to \mathcal{J}^+ . Another wavefront, B , is emitted and is marginally trapped until it is refocused into $r = 0$ (now labeled E) by the

thin shell of matter. A wavefront emitted previously, C , has positive divergence until it is refocused by the matter shell. At the instant C is refocused by the shell of matter and becomes marginally trapped, it is the outermost marginally trapped surface, now labeled D . Since no more matter falls on the star, C and D constitute the event horizon. The apparent horizon is defined by the surface B and D . The apparent horizon moves outward discontinuously while the event horizon moves outward continuously. It will be of interest to us later that the apparent horizon is guaranteed to lie within or coincide with the event horizon [34].

3.2 Apparent Horizon Equation

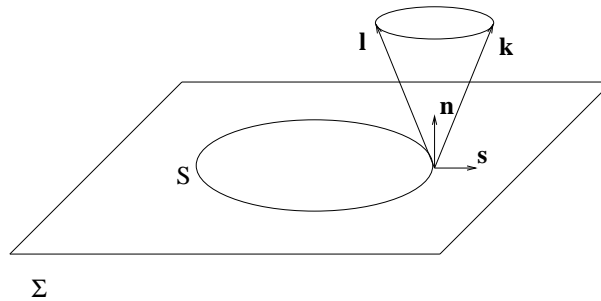


Figure 3.3: Representation of a 2-Sphere embedded in a hypersurface, Σ .

The previous section described the nature of the apparent horizon, now I present a mathematical definition [21,64]. Let S be a surface with S^2 topology and an outgoing null vector, k^a . Assume that S is a marginally trapped surface such that

$$\nabla_a k^a = 0. \tag{3.1}$$

The vector k^a can be written in terms of an outward pointing, spacelike normal to S , s^a ; and a future directed, timelike normal to $\Sigma(t)$, n^a :

$$k^a = s^a + n^a. \quad (3.2)$$

We also define an ingoing null vector l^a :

$$l^a = -s^a + n^a. \quad (3.3)$$

Note that eqns. (3.2) and (3.3) differ from York by $1/\sqrt{2}$. Similarly to the 3+1 decomposition of spacetime into space and time, the 3-metric, γ_{ab} , is projected onto S inducing a 2-metric h_{ab} via:

$$h^{ab} = \gamma^{ab} - s^a s^b. \quad (3.4)$$

In terms of the spacetime metric, g_{ab} , h_{ab} is

$$h^{ab} = g^{ab} + n^a n^b - s^a s^b, \quad (3.5)$$

where h_{ab} has indices raised and lowered by γ^{ac} of g^{ac} .

Eqn. (3.5) can be rewritten as:

$$h^{ab} = g^{ab} + l^{(a} k^{b)}. \quad (3.6)$$

This allows the divergence of k^a to be computed on the two surface using only h^{ab} ,

$$\nabla_a k^a = g^{ab} \nabla_a k_b = h^{ab} \nabla_a k_b + (l^{(a} k^{b)}) \nabla_a k_b. \quad (3.7)$$

The last term in eqn. (3.7) is $\frac{1}{2}[l^a(\nabla_a k_b)k^b + (k^a \nabla_a k_b)l^b]$. Of the two terms in the bracket, the first can be rewritten $\frac{1}{2}l^a \nabla_a (k_b k^b) = 0$ since k^a is null. The second term in the bracket computes the geodesic equation in k_a : this vanishes

since every null vector is tangent to some affinely parametrized, null geodesic so $k^a \nabla_a k_b = 0$.

Hence the divergence of the null field, $\nabla_a k^a$ is a 2-tensor, i.e. it is a tensor intrinsic to the 2-sphere and does not depend on how S is embedded in $\Sigma(t)$. Thus $\nabla_a k^a = h^{ab} \nabla_a k_b = h^{ab} \perp \nabla_a k_b = h^{ab} D_a k_b$ and only the spatial components of k_a and D_a need be computed. Equivalently,

$$\nabla_a k^a = h^{ab} \nabla_a (s_b + n_b) \quad (3.8)$$

$$= h^{ab} \perp \nabla_a (s_b + n_b) \quad (3.9)$$

$$= h^{ab} D_a (s_b + n_b) \quad (3.10)$$

where we have used eqn. (3.2). Since $K_{ab} = -D_a n_b$ (eqn.2.17) and eqn. (3.5),

$$\nabla_a k^a = h^{ab} (D_a s_b - K_{ab}) \quad (3.11)$$

$$= (g^{ab} + n^a n^b - s^a s^b) (D_a s_b - K_{ab}). \quad (3.12)$$

However, $D_a s_b - K_{ab}$ is spatial:

$$(D_a s_b - K_{ab}) n^a n^b = 0, \quad (3.13)$$

thus reducing eqn. (3.12) to

$$\nabla_a k^a = D^a s_a - s^a s^b D_a s_b - K + s^a s^b K_{ab}. \quad (3.14)$$

One further simplification to eqn. (3.14) due to the fact that $s^b D_a s_b = D_a (s^b s_b)/2 = D_a(1)/2 = 0$ leads to

$$\kappa \equiv \nabla_a k^a = D^a s_a - K + s^a s^b K_{ab}. \quad (3.15)$$

For a marginally trapped surface

$$\kappa = D^a s_a - K + s^a s^b K_{ab} = 0. \quad (3.16)$$

Eqn. (3.16) is called the apparent horizon equation since it describes the apparent horizon when the marginally trapped surface is outermost.

Solving eqn. (3.16) is equivalent to finding a surface that is marginally trapped, the outermost of which at any given time is the apparent horizon. The S^2 (spherical) topology of the apparent horizon naturally lends itself to characterization via spherical coordinates. The function,

$$\psi = r - h(\theta, \phi) \tag{3.17}$$

is a level set of 2-spheres in Σ , and the apparent horizon is the surface $\psi = 0$. The apparent horizon equation in spherical coordinates $(h(\theta, \phi), \theta, \phi)$ is a 2-dimensional problem in θ and ϕ . The function $h(\theta, \phi)$ is called the apparent horizon shape function.

We are interested in finding a *set of surfaces parameterized by κ* in Σ . The set of such surfaces characterized by κ will be a fundamental idea in our level flow method of locating apparent horizons. One can imagine a level set consisting of a series of surfaces embedded in a given hypersurface. Each surface has a different value of κ everywhere on it. This is equivalent to permeating the space with surfaces of constant expansion, outgoing null generators. The apparent horizon is recovered from the set of surfaces when $\kappa = 0$. Incidentally, the foliation of the 3-space in terms of constant κ surfaces is a geometrical basis for coordination and gauge choice (this is a subject for future investigation).

3.3 Apparent Horizon Excision

Solving the apparent horizon equation (eqn.(3.16)) for the outermost marginally trapped surface will identify the location of the apparent horizon in a single hypersurface. The spacetime is foliated by hypersurfaces so an apparent horizon finder must be used on each hypersurface for each desired horizon position. Once the horizon surface is located, the evolution code uses this information to avoid computing near the singularity. Apparent horizon excision uses the apparent horizon location to determine the region of the grid to be masked. The procedure requires no set of prescribed boundary conditions.

Apparent horizon excision is one of the most difficult aspects of a computational black hole simulation. The tracking of apparent horizons is not yet automatic in the evolution code. Initially, we use a linearly extrapolated estimate of the positions of the apparent horizons, and then we correct this estimate after running the level flow apparent horizon tracking code with the evolution data. The scheme for excising the singularity from the computational domain is the same whether or not apparent horizon tracking is turned on during evolution. The code has a function called the mask which is a series of 0's and 1's indicating which points in the domain are to be excised (mask=0) and which are not (mask=1). A buffer zone of a few grid points is used to ensure that the excised points are within the apparent horizon.

The mask function indicates which points are to be used in finite difference molecules. As discussed in Chapter 1, the molecules are centered around each grid point. The points on the border of the mask do not have equal numbers of points to each side. The differencing is designed to make intelligent decisions in choosing an extended, offset molecule to ensure second order

accuracy; and, more importantly, to ensure stability.

Chapter 4

Methodology

In this chapter, I describe the level flow method used to develop the apparent horizon tracker. In order to evaluate the level flow method, I suggest the following criteria for apparent horizon trackers:

- (1) The robustness of the tracker due to its lack of dependence on changes to the initial guess;
- (2) The generality of the tracker in its applicability to generic spacetimes including multiple back hole spacetimes; and
- (3) The efficiency of the tracker algorithm in CPU time.

I will refer to this list when comparing and contrasting the level flow method with other methods; and when identifying the strengths and weaknesses of the level flow method.

4.1 Algorithms for Finding Apparent Horizons

The first algorithms for locating apparent horizons were successful in spherically and axially symmetric spacetimes. Current methods involve three-dimensional codes to track apparent horizons in non-symmetric spacetimes. Most modern horizon locator codes in the literature are capable of finding the location of an apparent horizon in a generic, *single* black hole spacetime, and a few are capable of finding *multiple* apparent horizons in the special case of time-symmetric spacetimes.

For the spherically symmetric hypersurface with line element:

$$ds^2 = a^2 dr^2 + r^2 b^2 (d\theta^2 \sin^2 \theta d\phi^2), \quad (4.1)$$

eqn. (3.16) reduces to a one-dimensional, non-linear, ordinary differential equation:

$$\frac{d(rb)}{dr} - arbK_\theta^\theta = 0, \quad (4.2)$$

where coefficients a and b are functions of the coordinates and rb is the areal radius. Eqn. (4.2) can be solved by finding its zeros [20, 50, 4 55]. In axisymmetry, the apparent horizon equation reduces to a nonlinear, two-point, boundary value ordinary differential equation solved by shooting methods [18,8]. Most solutions of the apparent horizon equation in three dimensions fall into one of three categories: 1) The use of Newton's method to solve the apparent horizon equation as a boundary value problem, 2) The use of a pseudospectral expansion to integrate the apparent horizon equation, and 3) The use of curvature flow to rewrite the apparent horizon equation as a parabolic equation of motion within an artificial time, λ , which leads to the apparent horizon surface in the limit $\lambda \rightarrow \infty$.

The apparent horizon equation is a second order, elliptic equation. A prototypical elliptic equation is the Poisson equation:

$$\frac{\partial^2 u}{\partial x^2} + \frac{\partial^2 u}{\partial y^2} = \rho(x, y)$$

[51]. Elliptic equations are solved using a boundary value. For the apparent horizon equation, the boundary conditions on the horizon's shape enforce the smoothness of the surface across the boundary. One then typically solves the elliptic equation using finite difference techniques. The apparent horizon equation is non-linear; therefore, the algebraic equations resulting from the discretization are typically solved using Newton's method. Efficiency is an issue especially considering the storage requirements for solving large sets of equations. Jonathan Thornburg and Mijan Huq [38,59] have written successful boundary value routines to track apparent horizons. Their codes are fast (criterion 3) compared with codes using flow methods but require a good initial guess (criterion 1) and are not generalized for spacetimes with multiple black holes (criterion 2).

The second method is an algorithm based on a pseudospectral expansion of the apparent horizon shape function, $h(\theta, \phi)$ (eqn. (3.17)) in spherical harmonic basis functions:

$$h(\theta, \phi) = \sum_{l=0}^{l_{max}} \sum_{m=-l}^l a_{lm} Y_{lm}(\theta, \phi). \quad (4.3)$$

A finite number of the coefficients, $\{a_{lm}\}$ parameterize the horizon shape function, and the maximum l_{max} depends on the computation. The apparent horizon equation can then be solved by writing it as

$$\|\kappa(a_{lm})\| = 0, \quad (4.4)$$

and using a minimization routine to find a minimum of $\|\kappa\|$, typically not equal to, but close to, zero [25,14, 23]; or using a functional iteration scheme to solve $\kappa(a_{lm}) = 0$ for $\{a_{lm}\}$ [46]. This scheme has been implemented in generic, single black hole spacetimes but not in multiple hole spacetimes. Pseudospectral methods can be very fast (criterion 3) but their speed and memory storage depend on l_{max} . Kemball and Bishop [40] reported a dependency of l_{max}^4 in distorted cases and l_{max}^2 in spherical cases. In either case, the performance decreases with increasing distortion of the surface (criterion 1). This method has not been generalized to multiple holes (criterion 2).

The curvature flow approach, first applied to apparent horizons by K.P. Tod [60], is to rewrite the apparent horizon equation as a parabolic equation with a speed given by the expansion of the two-surface S in Σ . In the case of a time symmetric hypersurface, $K_{ab} = 0$, the apparent horizon equation reduces to the condition for a minimal surface, $D_a s^a = 0$. In this case, the surface, S , is at a local extremum of area. The variation of S along the spacelike normal to a minimal surface leaves the area unchanged as S is moved along a vector field, V^a

$$\partial A = - \int_S V^a H_a dS \quad (4.5)$$

where A is the area and H_a is the mean curvature vector. The minimal surfaces in Σ may be found by using a mean curvature flow [9,37,29] in which a starting surface, S_o , is parameterized by coordinates x^a and evolved in terms of a parameter λ . The equation is evolved by:

$$\frac{\partial x^a}{\partial \lambda} = -H s^a \quad (4.6)$$

where $\partial x^a / \partial \lambda$ is a vector field, and H is the mean curvature, which is the

trace of extrinsic curvature associated with embedding S in Σ given by

$$H = D_a s^a. \quad (4.7)$$

Eqn. (4.6) is the gradient flow for the area functional. The area decreases monotonically with increasing λ . Grayson [32] has shown that a surface deforming under its gradient field (eqn. (4.6)) will evolve to a stable minimum surface (surface is local minimum of area) if there is one, or to a point.

I am interested in the non-time symmetric case ($K_{ab} \neq 0$) for which the marginally trapped surfaces differ from minimal surfaces, the surfaces are not extrema of the area. However, Tod suggests an equation similar to eqn. (4.6) as a curvature flow:

$$\frac{\partial x^a}{\partial \lambda} = -\kappa s^a \quad (4.8)$$

using $\kappa = D_a s^a + s^a s^b K_{ab} - K$ as in eqn. (3.16). I have found it to be successful at identifying apparent horizons in generic hypersurfaces [56]. The curvature flow method fulfills the requirement of a robust algorithm (criterion 1). However, it is slow (criterion 3) and does not immediately apply to spacetimes containing multiple black holes (criterion 2).

The above methods have been very successful at detecting single apparent horizons. However, none are capable of detecting multiple apparent horizons without running the code more than once with different initial guesses. In general, the locations of singularities are not known prior to the evolution, so a method able to detect multiple apparent horizons from a single initial guess is desired. In an effort to find a method capable of detecting multiple horizons, Laguna [41] suggested a method called the level set method by Osher and Sethian [47]. The level set method is an algorithm capable of following fissioning surfaces in Euclidean spacetimes. It embeds the surface, ϕ , into a

higher dimensional surface, Φ . The original surface is set as the zeroth level of Φ , $\Phi = 0 = \phi$. Figure (4.1) depicts an example to illustrate the embedding of the guess surface into a higher dimensional surface, in the case a circle embedded into a paraboloid.

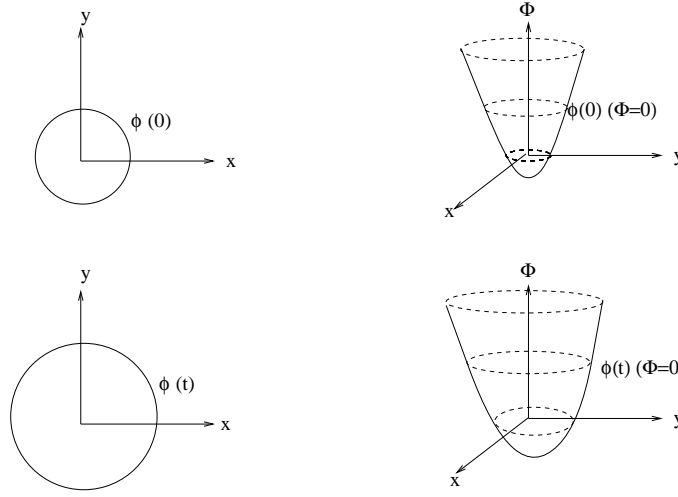


Figure 4.1: An example illustrating the embedding of a series of surfaces, ϕ into a higher dimensional surface, Φ . The surface of interest is reclaimed by setting $\Phi = 0$.

Φ is evolved under a curvature flow equation of motion where the velocity is the local mean curvature of ϕ embedded in Φ . The reason this method can successfully follow a surface undergoing fission while the curvature flow method can not is that the equation of motion is flowing the Φ not ϕ . Φ is not fissioning. The final surfaces are found by setting Φ at the final time to zero. An example of where multiple apparent horizons would exist in the final Φ solution is illustrated in fig. (4.2).

In Euclidean spacetimes, the mean curvature of embedding ϕ into Φ is known [47] and the mean curvature flow method is used to determine the

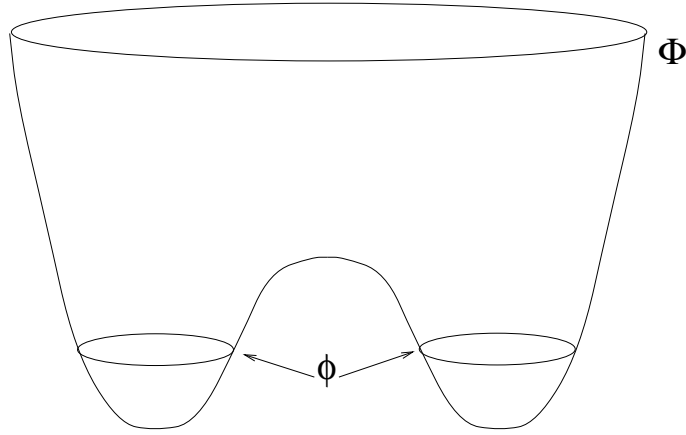


Figure 4.2: The level set method in theory would find the two apparent horizons by flowing the $N + 1$ -dimensional surface. ϕ is identified at $\Phi = 0$.

equation of motion. For generic, pseudo-Riemannian spacetimes, the determination of a mean curvature for embedding ϕ in Φ is difficult. Pasch [48] found the mean curvature for a time-symmetric spacetime and successfully implemented the level set method for that particular case but not in general; therefore failing to meet criterion 2. The level set method has an added dimension and is therefore expensive (criterion 3). Here I implement an alternate method to detect topology change.

4.2 Level Flow Method

The level flow method can detect the change in topology of a guess surface and predict the resulting multiple surfaces in generic, multi-hole spacetimes. The level flow method is designed to flow the trial surface, ψ , through a fission into two surfaces. To detect fission in the trial surface, I begin by flowing ψ with an equation similar to the curvature flow equation, eqn. (4.8). Eqn. (4.8)

can be reset into an equation on the trial function ψ which is “evolved” in λ to finally find the apparent horizons as $\psi = 0$. Since $\frac{\partial\psi}{\partial\lambda} = \frac{\partial x^a}{\partial\lambda} \frac{\partial\psi}{\partial x^a}$ by the chain rule, multiply eqn. (4.8) by $\frac{\partial\psi}{\partial x^a}$ gives

$$\frac{\partial\psi}{\partial\lambda} = -\kappa s^a \frac{\partial\psi}{\partial x^a}. \quad (4.9)$$

Using

$$s^a = g^{ab} \frac{\frac{\partial\psi}{\partial x^b}}{\|\nabla\psi\|} \quad (4.10)$$

and

$$\|\nabla\psi\| = \sqrt{\frac{\partial\psi}{\partial x^a} \frac{\partial\psi}{\partial x^b} g^{ab}} \quad (4.11)$$

the test surfaces flow is given by:

$$\frac{\partial\psi}{\partial\lambda} = -\kappa \|\nabla\psi\|. \quad (4.12)$$

Eqn. (4.12) will flow the test surface, ψ , to a marginally trapped surface at $\psi = 0$ at when $\kappa = 0$; however, I wish to flow to a set of surfaces defined by $\kappa = c_n$, where $n = 1, 2, \dots$. The integer n acts as a counter for the number of surfaces in the set. To accomplish this, I modify the flow equation to accommodate this more general flow

$$\frac{\partial\psi}{\partial\lambda} = -F(\kappa) \|\nabla\psi\|, \quad (4.13)$$

where $F(\kappa)$ is a speed function.

The ability to fission the surface depends on the choice of the speed function. In the traditional curvature flow method (eqn. (4.8)), the speed function is chosen to be $F(\kappa) = \kappa$, a good choice since $F(\kappa) = \kappa = 0$ is a marginally trapped surface. However, this choice will not flow ψ through a fission; in general the finite difference scheme fails as the surface pinches. The

level set method avoided this difficulty by flowing an $N+1$ -dimensional surface, Φ , that did not fission. In contrast, I choose to flow an N -dimensional surface, ψ , but use the one-parameter family of surfaces in Σ I call the level set $S(c_n)$ to indicate a fission. The level set is a collection of constant κ values given by c_n in $\Sigma(t)$. In future work, these surfaces will be used in a coordination of $\Sigma(t)$.

I choose a $F(\kappa) \propto \kappa - c_n$. This speed function allows flow to multiple surfaces in the set as $\kappa - c_n = 0$. As $\kappa - c_n \rightarrow 0$, I am solving for a particular surface in the level set, $S(c_n)$. This surface has a constant value of $\kappa = c_n$ everywhere on it. A set of surfaces is found by varying c_n as the flow progresses

$$c_{n+1} = c_n \pm \Delta c, \quad (4.14)$$

where (+) in outward flow and (-) in inward flow and $\Delta c \propto \|\kappa\|_2$.

Eqn. (4.8) is a general equation with the speed function, F , made to suit our purpose of tracking apparent horizons. To locate surfaces in Σ parametrized by κ , I choose two options for the speed function:

$$F(\kappa) = \kappa - c_n \quad (4.15)$$

$$F(\kappa) = (\kappa - c_n) \arctan^2\left(\frac{\kappa - c_n}{\kappa_o}\right). \quad (4.16)$$

Both functions flow the trial surface ψ to a surface $S(c_n)$. The second function, eqn (4.16), behaves similarly to the first but allows for larger time steps near a fissioning surface because it moves points further from the eventual solution faster than the points closer to the eventual solution. A more detailed description is given in the next chapter.

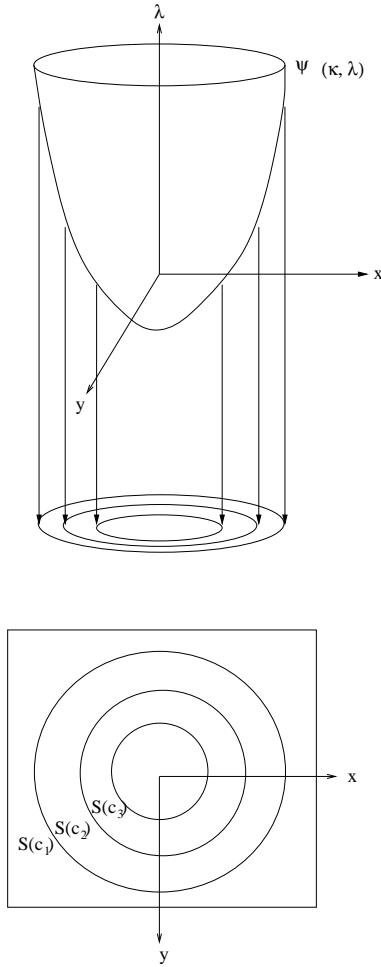


Figure 4.3: Schematic of $\psi(c_n)$, the level set of surfaces in $\Sigma(t)$. I solve for a single surface, $S(c_n)$, in $\psi(c_n)$. Multiple levels are used in detecting the existence of multiple horizons.

The only information needed to initiate the level flow code is the 3-metric and extrinsic curvature components of the hypersurface plus the starting radius and center of the guess surface. γ_{ab} and K_{ab} are generated by evolution codes or closed form solutions of the 3+1 equations. The starting surface radius and center are input parameters to initialize a topological 2-sphere that

acts as the deforming trial surface. The radii and center do not have to be particularly good initial guesses (criterion 1). As the flow velocity approaches zero, $F(\kappa - c) \rightarrow 0$, $\kappa \sim c_n$ and a surface $S(c_n)$ is found within a tolerance (ϵ_κ). When $\kappa = 0$, the located surface describes a marginally trapped surface. If the surface is the outermost marginally trapped surface in the hypersurface, it is the apparent horizon. To ensure that the surface is the apparent horizon, the starting surface should enclose the suspected horizon area i.e., start outside.

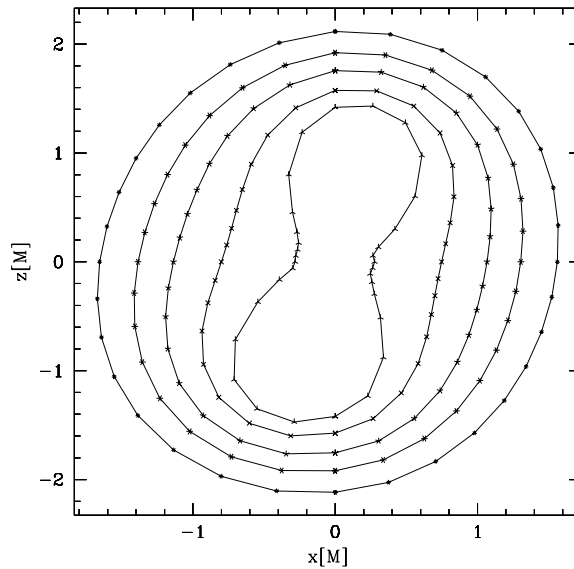


Figure 4.4: Plot of five levels ($\kappa = 0.14, 0.12, 0.10, 0.08, 0.06$) of constant divergence of outgoing null geodesics.

I use this level set parametrized by c_n to determine if the topology is changing in the surface. Fig.(4.4) shows the level set found in a spacetime containing two black holes with coordinate locations $(-0.954, 0, -0.3)M$ and $(0.954, 0, 0.3)M$. Each 2-surface has a constant value of κ . I monitor the topology of the deforming surface by computing the radial component of the

gradient of κ with respect to the normals of each surface in the level set. The gradient is defined as:

$$\frac{|\kappa_{n-1} - \kappa_n|}{|r_{n-1} - r_n|}, \quad (4.17)$$

where r is the radial function given in eqn. (3.17). A sharp increase in the gradient indicates the existence of multiple surfaces. To ensure that I do not erroneously abandon a single surface, I also monitor the maximum of the l_2 -norm of κ . If κ is no longer decreasing, I am no longer finding a solution to eqn. (3.16); otherwise the single surface is retained. The level flow method is essentially a special set of surfaces with properties that let us determine when to break. If I only flowed to $\kappa = 0$, I would not form the collection of $\kappa = \text{constant}$ surfaces.

Once a topology change is indicated, the radii and centers for each of the new surfaces are found (note that these four parameters for each surface are all that is needed). To find these two new centers and radii, the center of the final single surface (from which I break) is calculated and the minimum of the expansion gradient is determined. These two pieces of information are used to create a vector that introduces a direction and its negative into the situation, fig. (4.5). With a direction, the new center and radius are found using the points associated with the solid arrow for one surface and the points with the dotted arrow for the second surface. The tracker then flows the two new surfaces depicted rightmost in fig. (4.5) until $\kappa = 0$ within an ϵ_κ .

The level flow method is applicable to generic, multiple black hole space-times (criterion 2) and can detect apparent horizons from a single reasonable guess (criterion 1). The drawbacks of the level flow method is the dependence of $\Delta\lambda$ on the spatial grid size, $\Delta\lambda \sim N^{-2}$ where $N^2 = N_\theta N_\phi$ is the number of grid points, and the fact that I flow to a speed of zero (the flow

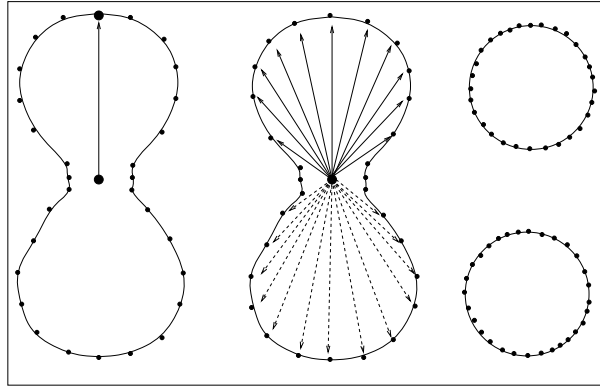


Figure 4.5: Two-dimensional schematic representation of the three-dimensional decision process to identify the two surfaces that will evolve to the two apparent horizons. The last figure on the right depicts the final two surfaces that will act as new test surfaces.

speed approaches zero as κ approaches zero). Work is in progress to improve the speed of this algorithm (criterion 3). Improvements have been made to increase the efficiency of the current algorithm. The addition of the \arctan^2 function, eqn. (4.16), speeds up the algorithm during the fissioning process. A further development has been the addition of an adaptive λ -step routine that monitors the number of λ -iterations taken to solve in each λ -step of the process, and alters the λ -step accordingly. These improvements will be explained in detail in the following chapter on code development.

Chapter 5

Code Development

5.1 The Equation of Motion

The apparent horizon tracker is a program that uses the level flow method to solve the apparent horizon equation eqn. (3.16). The level flow method code solves eqn. (3.16) on each spacelike hypersurface of the foliated spacetime by iterating the equation of motion, eqn. (4.13) with eqn. (4.11) and speed function, eqn. (4.16). Typical flow methods, as applied to the apparent horizon problem in general relativity, flow the trial surface, S_o , under eqn. (4.13) to a single surface, the apparent horizon. In the level flow method, I flow the trial surface to a set of surfaces containing the apparent horizon, (S_{c_n}) . (S_{c_n}) fill the hypersurface and contain information on topology changes I use to search for the apparent horizons.

As previously mentioned, the code needs only the components of the dynamical variables γ_{ij} and K_{ij} to initiate. Since our dynamical variables have been determined by an evolution code in Cartesian coordinates and the

apparent horizon code uses spherical coordinates to characterize the 2-surfaces, the components of the 3-metric and extrinsic curvature are interpolated onto the 2-surface. The interpolation scheme in the level flow algorithm was written by Mijan Huq [38].

The equation of flow is computationally solved using a finite difference scheme called the Crank-Nicholson method. The advantage of the Crank-Nicholson method is in its combination of an implicit scheme for stability and an explicit scheme for accuracy to second order. The Crank-Nicholson method is used often for diffusive initial value problems. Fig. 5.1 depicts the molecule used in the Crank-Nicholson method.

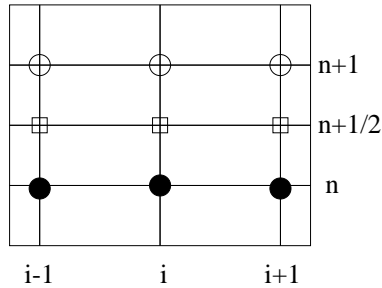


Figure 5.1: The Crank-Nicholson scheme averages explicit and implicit methods resulting in a second order accurate scheme that is usually stable at large λ -steps. The filled in circles are the values used to determine the values at the empty circles. The empty squares are intermediate values.

For the level flow method, the finite difference equation is

$$\psi_{i,j}^{n+1} = \psi_{i,j}^n - \frac{4\Delta\lambda}{\pi^2} (\kappa_{i,j}^n - c) (\arctan(\kappa_{i,j}^n - c) / \kappa_o)^2 |\nabla \psi_{i,j}^n|. \quad (5.1)$$

For convenience, I define R^n to be equivalent to the right hand side of eqn. (5.1). Eqn. (5.1) is non-linear making traditional methods of inverting the resulting matrix to solve the Crank-Nicholson method difficult. Instead, I implement

an iterative Crank-Nicholson scheme shown below in pseudocode format:

```

While  $\kappa > \epsilon_\kappa$  Do  $1 \rightarrow \lambda_{max}$ 
  Store  $\psi_{old}^{n+1} = \psi^{n+1}$ 
  While  $\| \psi^{n+1} - \psi_{old}^{n+1} \| > \epsilon_{tolerance}$ 
    Store  $\psi_{old}^n = \psi^{n+1}$ 
    Average  $\psi^{n+1/2} = (\psi^{n+1} + \psi^n) / 2$ 
    Interpolate  $g_{mn}$  and  $k_{mn}$  onto 2-Surface
    Evaluate  $R^{n+1/2}$  using  $\psi^{n+1/2}$ 
    Update  $\psi^{n+1} = \psi^n + \Delta t R^{n+1/2}$ 
  End While
  Save  $\psi^n = \psi^{n+1}$ 
End While

```

Iterated Crank-Nicholson converges to an exact solution of the implicit problem. However, the detailed behavior of this convergence [57] shows that the Crank-Nicholson solution at a particular iteration has an amplification factor $|\mathcal{A}^{(n)}|$ that oscillates around unity. The behavior varies in pairs: $|\mathcal{A}^{(n)}| < 1$ for $n = 2, 3$; $|\mathcal{A}^{(n)}| > 1$ for $n = 4, 5$, etc. while $|\mathcal{A}^{(n)} - 1| \rightarrow 0$ monotonically as $n \rightarrow \infty$. n is counting the number of iterations it takes to get $\hat{u} = u$ within the specified $\epsilon_{tolerance}$. I maintain a Crank-Nicholson iteration of $n = 2$ or $n = 3$. In the runs I show in the following chapters, $\epsilon_{tolerance} = 10^{-6}$ and $\epsilon_\kappa = 10^{-4}$. The value of $\epsilon_{tolerance}$ determines how small the error is in the iterative Crank-Nicholson scheme, and is kept less than h^2 .

The iterative Crank-Nicholson method provides a method of estimating the rapidity of convergence, since one can count the number of Crank-Nicholson iterations. If the iterations exceed 3, I reduce the overall Courant

factor, η , by $0.1\Delta\lambda$, i.e. $\Delta\lambda \rightarrow 0.9\Delta\lambda$. Similarly, if the number of Crank-Nicholson iterations drop to 1, I increase η by $0.1\Delta\lambda$.

Driving the value of ϵ_κ down to machine precision is difficult in the flow equation since the speed of the flow depends on κ . The role of the apparent horizon tracker as a locator of apparent horizons for the purpose of masking the singularity does not require $\kappa = 0$ to high precision. In fact, a trapped surface with $\kappa < 0$ would suffice. However, when investigating properties of the apparent horizons, specifically the area of the apparent horizon, the uncertainty in the area is proportional to the uncertainty in κ . Future generations of our horizon tacking code will have new ways of driving the ϵ_κ down. Such issues are addressed in Chapter 8. One way I am already using to drive ϵ_κ down is the arctan function in the equation of motion. The effect is to shrink the size of $\Delta x^2/\Delta\lambda$ as $\kappa \rightarrow 0$, where $\Delta x = h$. Fig. (5.2) contains a couple of plots produced using MapleV. The plot of the left is the function $g(x) = x - c$, where $c = 0$. The plot on the right is the function $f(x) = 4(x - c)/\pi^2 \arctan^2((x - c)/x_o)$ where $c = 0$ and $x_o = 0.02$. The arctan function acts like a break during the region close to zero but behaves linearly far from 0. A blow-up of the behavior of $f(x)$ close to 0 is shown in fig. (5.3). The solution to $f(x) = 0$ is $x = 0$, the functional dependence I require in our speed function.

5.2 Convergence Tests

To test the level flow method, I follow Choptuik's [20] treatment of tests for accuracy of finite difference schemes. We are numerically solving a continuum partial difference equation with finite differencing. We have a continuum

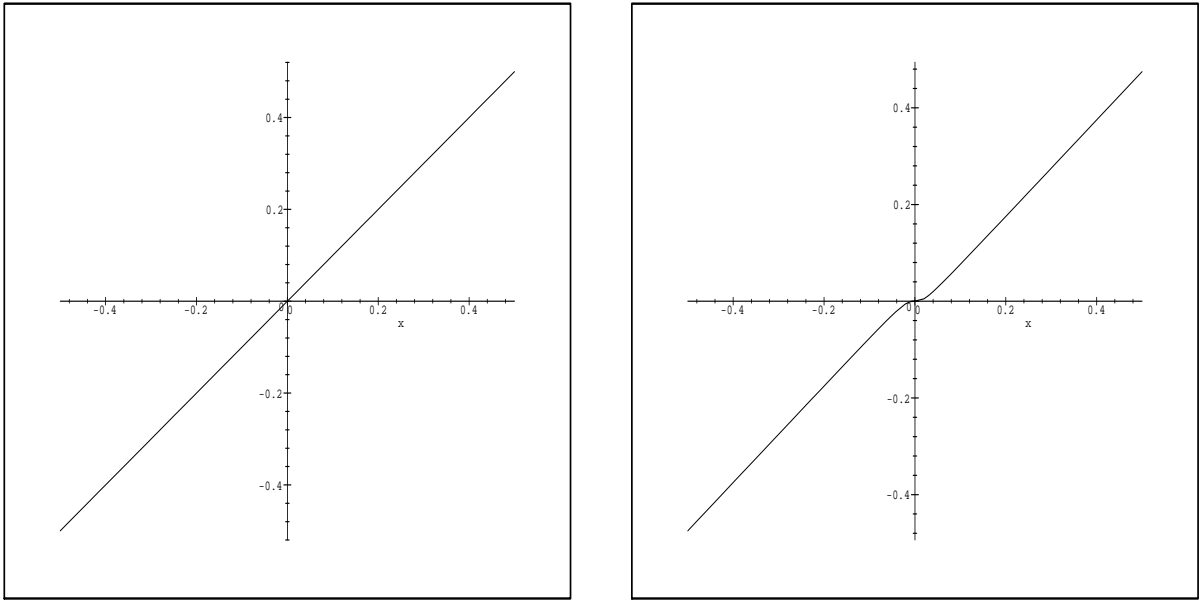


Figure 5.2: The plot on the left is the function $g(x)$ and the plot on the right is function $f(x)$. Note the flattening out of the slope in $f(x)$ that I use to control the λ -evolution of the surface near breaking.

function, u , and a discretized function, \hat{u} . Given a differential operator, L , the continuum partial differential equation can be written as:

$$Lu = 0. \tag{5.2}$$

When solving this equation via finite differencing, I incur two errors, the truncation error

$$\hat{\tau} \equiv \hat{L}\hat{u}, \tag{5.3}$$

and the solution error

$$\hat{e} \equiv u - \hat{u}. \tag{5.4}$$

The scheme is p order accurate if $\hat{\tau} = O(h^p)$. We will be dealing with a second order scheme so $p = 2$. As $h \rightarrow 0$ I assume that the discretized function can

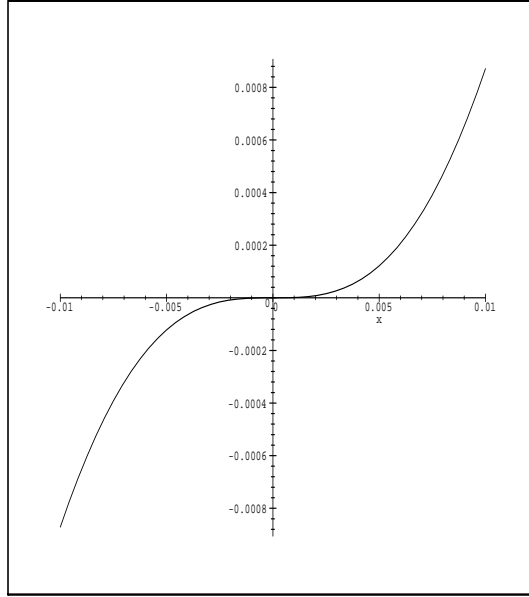


Figure 5.3: The function $f(x)$ is zoomed in on region of interest.

be expressed:

$$\hat{u} = u - h^2 e_2 - h^4 e_4 - \dots, \quad (5.5)$$

where e_i are independent of the grid spacing, h . To check the convergence of the finite difference scheme, I need at least three different grid resolutions, h , $2h$, and $4h$ with corresponding functions \hat{u}_h , \hat{u}_{2h} , and \hat{u}_{4h} . Using eqn. (5.5), the following relations for the functions per resolution are obtained

$$\hat{u}_h = u - h^2 e_2 - h^4 e_4 - \dots \quad (5.6)$$

$$\hat{u}_{2h} = u - 4h^2 e_2 - 16h^4 e_4 - \dots \quad (5.7)$$

$$\hat{u}_{4h} = u - 16h^2 e_2 - 256h^4 e_4 - \dots \quad (5.8)$$

The convergence factor that I use to determine the accuracy of the scheme is

$$C_f \equiv \frac{\hat{u}_{2h} - \hat{u}_{4h}}{\hat{u}_h - \hat{u}_{2h}}. \quad (5.9)$$

For a second order scheme, the convergence factor in eqn. (5.9) is $C_f = 4 + O(h^2)$. By finding the convergence factor, I can determine whether or not I am correctly finite differencing the equation.

In the level flow method, the evolved function is

$$u \equiv \psi = r - h(\theta, \phi). \quad (5.10)$$

In order to verify that the code is obtaining second order accuracy, I have plotted the convergence factor versus the number of λ -steps for the updated variable, ψ as a function of θ as given in eqn. (5.10) for two different sets of data, a single Schwarzschild black hole and two Brill-Lindquist black holes. I also present the convergence factor for the discretized κ in the Schwarzschild case. The Schwarzschild and Brill-Lindquist data sets will be described in detail in the next chapter. The three different resolutions, h , $2h$, and $4h$, are obtained by changing the number of spatial grid points on the surface. The number of grid points, N^2 , is related to the spatial step size in the level flow method by

$$h = \Delta\theta^2 \propto \frac{1}{N}. \quad (5.11)$$

We change the resolution by changing N and keeping the Courant factor constant thus changing $\Delta\lambda$ proportionally as:

$$\Delta\lambda = \text{Courant factor} \times \Delta\theta^2, \quad (5.12)$$

where $\Delta\theta$ is the spatial grid step size.

For the first data set, a single Schwarzschild black hole, I show two convergence tests. Fig. (5.4) is a plot of the convergence factor, C_f , versus the number of iteration for $\psi(\theta)$. In this case I have a fine spatial resolution of $h = 0.05$, a medium resolution of $h = 0.10$, a course resolution of $h = 0.20$, and

a λ -step size of $\Delta\lambda = 0.0012$. Fig. (5.5) is a plot C_f versus λ for the expansion, κ as a function of θ . This plot shows a little jump in the convergence factor at $\lambda = 950$, this occurs when one of the surfaces in the level set has been found and the flow starts to find the next surface.

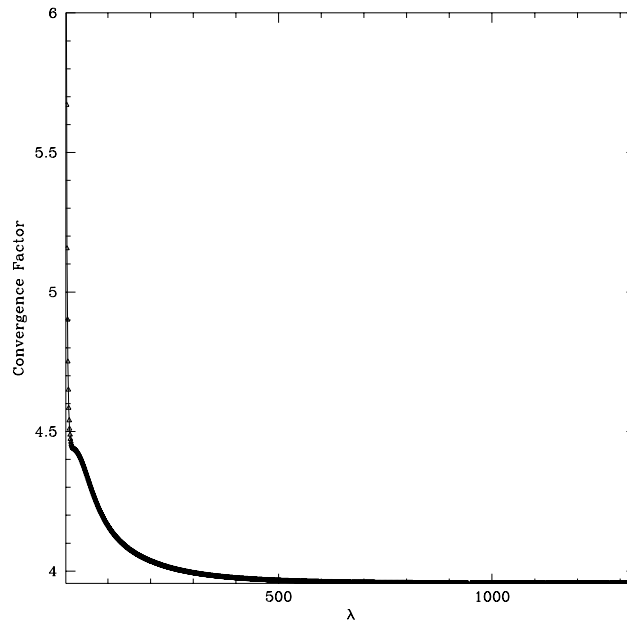


Figure 5.4: Convergence factor for radial variable ψ with $h = 0.05$, $2h = 0.10$, $4h = 0.20$, and $\Delta\lambda = 0.0012$ for Schwarzschild data. Second order accuracy is obtained.

The second case is for binary black hole data using Brill-Lindquist data. In fig. (5.6), the two holes are of equal mass and are separated by a distance equal to twice the mass of one of the holes. In fig. (5.6) the finest spatial resolution is $h = 0.05$ ($2h = 0.10$ and $4h = 0.20$) and the λ -step is $\Delta\lambda = 0.00012$.

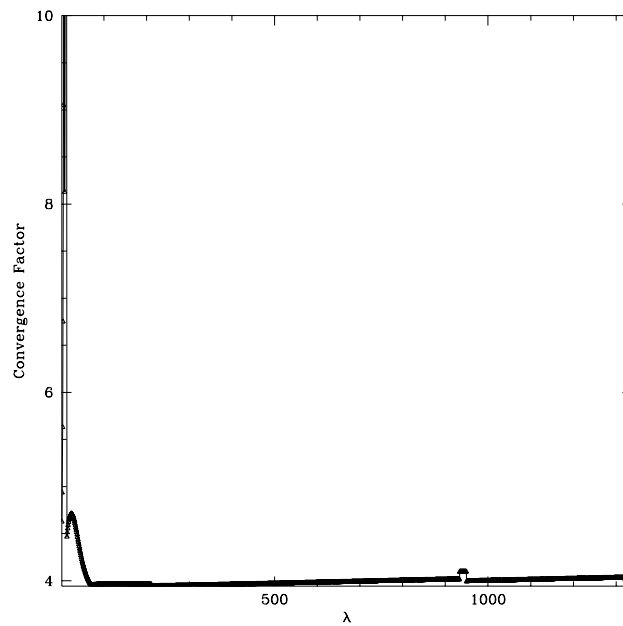


Figure 5.5: Convergence factor for $\kappa(\theta)$ in the Schwarzschild data with $h = 0.05$, $2h = 0.10$, $4h = 0.20$, and $\Delta\lambda = 0.0012$. Second order accuracy is again obtained, the jump at $\lambda = 950$ occurs when one surface of the level set is found and the flow starts again to find the next surface in the level set. of c_n is adjusted.

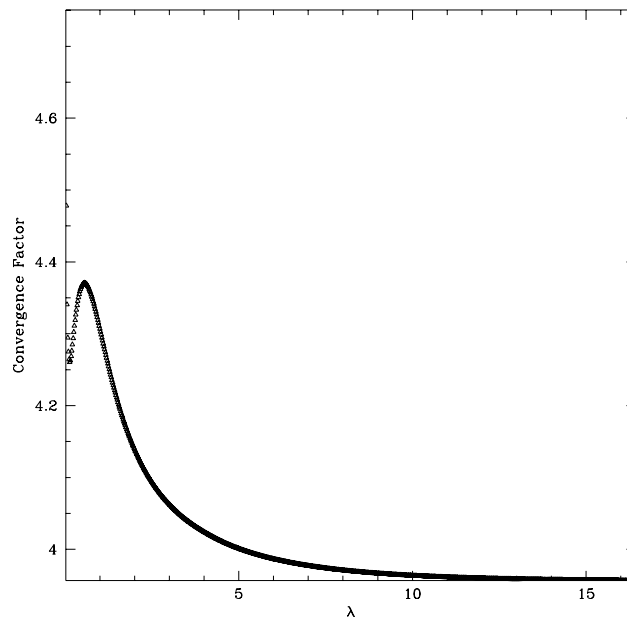


Figure 5.6: Convergence factor for radial variable ψ with $h = 0.05$, $2h = 0.10$, $4h = 0.20$, and $\Delta\lambda = 0.00012$ for the Brill-Lindquist data. The differencing scheme is second order accurate throughout the run.

Chapter 6

Apparent Horizon Tracking in Closed-Form Solutions of the Einstein Equation

The level flow method of tracking apparent horizons has been designed to locate apparent horizons in single and multiple black hole spacetimes. Starting from a reasonable initial surface, the surface deforms along the normals following the flow of the outgoing geodesics. To test the level flow tracker, I locate apparent horizons in Schwarzschild, Kerr, and Brill-Lindquist data. In particular, I also demonstrate the level flow method's ability to detect binary black holes in the Brill-Lindquist data.

6.1 Schwarzschild Data

The Kerr-Schild metric provides a closed-form description of both the Schwarzschild and the Kerr solutions to the Einstein equation and is given by:

$$g_{ab} = \eta_{ab} + 2Hl_a l_b, \quad (6.1)$$

where η_{ab} is the Minkowski metric, $\eta_{ab} = \text{diag}(-1, 1, 1, 1)$. H is a scalar function of the coordinates and l_a is an ingoing null vector with respect to both the Minkowski and full metrics; that is l_a satisfies the relation:

$$\eta^{ab}l_a l_b = g^{ab}l_a l_b = 0. \quad (6.2)$$

For the Schwarzschild solution, the metric given in eqn. (6.1) has the scalar function, H , given by:

$$H = \frac{M}{r} \quad (6.3)$$

and the components of the null vector are

$$l_t = 1 \quad (6.4)$$

$$l_x = \frac{x}{r} \quad (6.5)$$

$$l_y = \frac{y}{r} \quad (6.6)$$

$$l_z = \frac{z}{r} \quad (6.7)$$

where I have adopted rectangular coordinates (t, x, y, z) with $r = \sqrt{x^2 + y^2 + z^2}$, and M the mass of the black hole. The resulting line element is known as the Eddington-Finkelstein form of the Schwarzschild solution

$$ds^2 = - \left(1 - \frac{2M}{r}\right) dt^2 + \frac{4M}{r} dr dt + \left(1 + \frac{2M}{r}\right) dr^2 + r^2 (d\theta^2 + \sin^2 \theta d\phi^2). \quad (6.8)$$

In these coordinates we see that there is no singularity of any sort at $r = 2M$. The metric component g_{tt} vanishes at $r = 2M$ but the metric remains nonsingular - has a well defined inverse - there. The line element is well defined through the event horizon up to $r = 0$ where a true physical singularity resides.

We track the apparent horizon in this situation for a single black hole of mass, M . The closed form answer for the apparent horizon location is $r = 2M$ [45]. Fig. (6.1) shows the apparent horizon surface at slice $\theta = \pi/2$ with a solid line and $\phi = \pi$ with a dashed line; thus giving two circumferences of the horizon. Both circles should line up and do given the low resolution of 17^2 points on the sphere. A higher resolution plot, 33^2 points, is given in fig. (6.2). Here the slices appear almost as one. This shows the tracker can accurately find spherical horizons in this case.

The area of the event horizon for the Schwarzschild solution of the Kerr-Schild metric is given by [45]

$$A = 4\pi r_+^2 \tag{6.9}$$

where r_+ is the event horizon radius given by

$$r_+ = 2M \tag{6.10}$$

The event and apparent horizons coincide for these cases, assuming no dynamics. Using eqn. (6.10) and a numerically calculated radius, r_{num} , we find that $r_+ = 2.00M$ and $r_{num} = 2.007M$, resulting in a 0.35% error where the percent error = $((r_+ - r_{num})/r_+) \times 100$. The numerical radius, r_{num} is calculated using the maximum distance in the z -direction, the direction of spin. The area calculated using the eqn. (6.9) is $A = 16\pi M^2 = 50.265482M^2$. The apparent horizon tracker returns areas depending on the resolution of

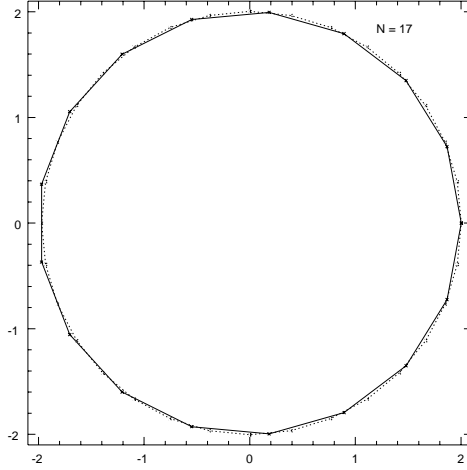


Figure 6.1: Apparent horizon located in Eddington-Finkelstein form of the Schwarzschild metric for a run with 17^2 grid points on the sphere. The solid line corresponds to $\theta = \pi/2$ slice and the dashed line the $\phi = \pi$ slice. The located horizon is close to spherical. the grid coordinates are given in units of M .

the grid, of $A_{num}(N = 17) = 50.11M^2$, $A_{num}(N = 33) = 50.23M^2$, and $A_{num}(N = 65) = 50.26M^2$, where N^2 is number of grid points on the surface. As expected, $A_{num} \rightarrow A$ as N increases. The area of a 2-surface is computed by:

$$A_{num} \equiv \int_S \sqrt{h} dx dy, \quad (6.11)$$

where h is the determinant of the 2-metric, h_{ab} , and x and y are coordinates. The numerical area is determined from eqn. (6.11) by calculating the determinant at every point in the grid and using a trapezoidal integration scheme [38].

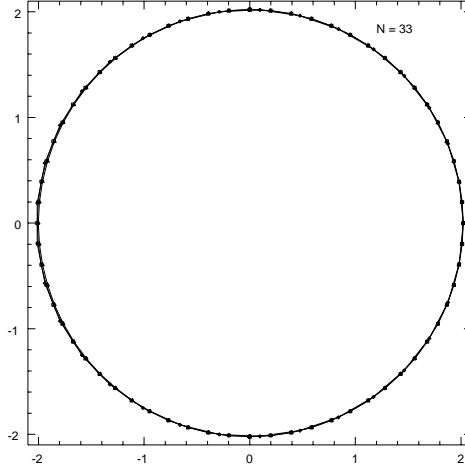


Figure 6.2: Apparent horizon located in Eddington-Finkelstein form of the Schwarzschild metric for a run with 33^2 points on the surface. The solid line corresponds to $\theta = \pi/2$ slice and the dashed line the $\phi = \pi$ slice. the two are impossible to distinguish at this resolution.

6.2 Kerr Data

The Kerr solution is a second solution given by the Kerr-Schild metric, eqn. (6.1).

The Kerr solution is the solution for a spinning black hole, *i.e.* a black hole with an internal angular momentum per unit mass given by a . In rectangular coordinates (t, x, y, z) , the scalar function and null vector are given by:

$$H = \frac{Mr^3}{r^2 + a^2z^2} \quad (6.12)$$

and

$$l_\mu = \left(1, \frac{rx + ay}{r^2 + a^2}, \frac{ry - ax}{r^2 + a^2}, \frac{z}{r}\right), \quad (6.13)$$

where $\mu = (t, x, y, z)$, M is the mass of the black hole, $a = J/M$ is the angular momentum per unit mass of the black hole in the z -direction, and r is obtained

from:

$$\frac{x^2 + y^2}{r^2 + a^2} + \frac{z^2}{r^2} = 1 : \quad (6.14)$$

$$r^2 = \frac{1}{2}(\rho^2 - a^2) + \sqrt{\frac{1}{4}(\rho^2 - a^2) + a^2 z^2}, \quad (6.15)$$

with $\rho = \sqrt{x^2 + y^2 + z^2}$.

The difference here is the addition of angular momentum. We test two cases, $a = 0.5M$ and $a = 0.9M$. Fig. (6.3) presents $a = 0$ again and the $a = 0.5M$ and $a = 0.9M$ cases. The solid line is again the $\theta = \pi/2$ slice and the dashed line is the $\phi = \pi$ slice. The expected result, that the deformation in the $\phi = \pi$ slice is increasing with a is found. The radius of the horizon is

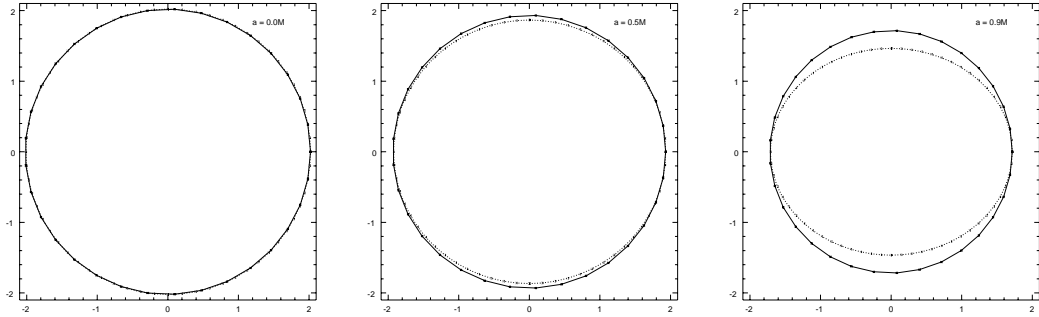


Figure 6.3: The three plots correspond to the location of the apparent horizons for black holes with three different values of angular momentum. The units of the graph are M , and the solid line is again the $\theta = \pi/2$ slice and the dashed line is the $\phi = \pi$ slice.

given by

$$r_+ = M - \sqrt{M^2 - a^2} \quad (6.16)$$

in the direction of the spin. The solution to eqn. (6.16) for $a = 0.5M$ is $r_+ = 1.8660M$ and the numerical solution we obtain for the horizon radius is $r_{num} = 1.8671M$, an error of 0.059%. In the $a = 0.9M$ case, $r_+ = 1.44M$ and

$r_{num} = 1.46M$, with a 1.39% error. The area of the horizon for each case can be calculated using

$$A = 4\pi(r_+^2 + a^2) \quad (6.17)$$

eqn. (6.9) and numerically using eqn. (6.11). In the $a = 0.5M$ case, eqn. (6.9) gives $A = 46.89M^2$, numerically I obtain $A_{num} = 46.88M^2$, resulting in a 0.21% error. In the $a = 0.9M$ case, $A = 36.09M^2$ and $A_{num} = 36.39M$ with a 0.83% error. The errors will decrease as ϵ_κ is driven closer to zero.

6.3 Brill-Lindquist Data

In this section, we study a binary black hole system using Brill-Lindquist data [14]. This data is useful to us for two reasons: We can verify previous results of the critical separation, and study an example of how the tracker works in finding multiple apparent horizons. The Brill-Lindquist data is probably the simplest multi-black hole data set. The 3-metric is time symmetric, $K_{ab} = 0$, and is conformally flat:

$$\gamma_{ab} = \psi^4 \eta_{ab} \quad (6.18)$$

where

$$\psi = 1 + \sum_{i=1}^N \frac{M_i}{2r_i} \quad (6.19)$$

and N is the number of holes ($N = 2$), M_i is the mass of i th the black hole and the r_i are the radial distances from the origin of the coordinate system to the centers, (c_{xi}, c_{yi}, c_{zi}) , of the black holes

$$r_i = \sqrt{(x - c_{xi})^2 + (y - c_{yi})^2 + (z - c_{zi})^2}. \quad (6.20)$$

We use isotropic coordinates to express the metric as

$$ds^2 = \psi^4 (dr^2 + r^2 d\theta^2 + r^2 \sin^2 \theta d\phi^2) \quad (6.21)$$

with

$$r_i = \sqrt{r^2 + d_i^2 - 2d_i r \cos \theta}, \quad (6.22)$$

where d_i is the distance between the holes and the center of the coordinate system. When they are far apart, each hole has an apparent horizon of radius $M/2$ in these coordinates. The area of each of the holes when they are well separated is $16\pi M^2$.

The limiting separation of the holes between single and double horizons was found by Brill and Lindquist [14] to be 1.56, Cadez 1.534 ± 0.002 [18] and [1.5,1.6] by Alcubierre et. al. [2]. We found a critical separation 1.53(5). The apparent horizon at the critical separation of 1.535 is shown in fig. (6.4) using the level flow code with 33^2 grid points.

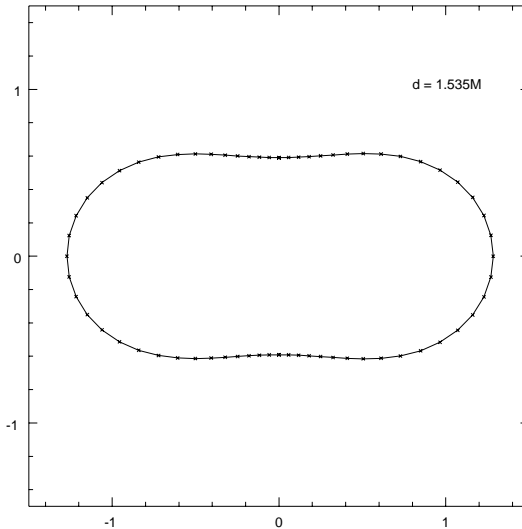


Figure 6.4: Separation of $1.535M$ with a 33^2 grid. The area was determined numerically to be $184.16M^2$

The horizon found for a separation, $d = 1.5$, less than the critical separation, is shown in fig. (6.5). Fig. (6.6) is a plot of the l_2 -norm of the maximum

of $\kappa(\theta)$ for the separation $d = 1.5M$ at each iteration plotted versus the number of λ -steps. This is one of the checks in the level flow code to ensure that the apparent horizon equation is still being solved. We expect the expansion to continue to decrease if we have started outside the apparent horizon and are flowing inward. As we will see in fig. (6.10), the expansion increases as fission occurs in a data set with separated holes.

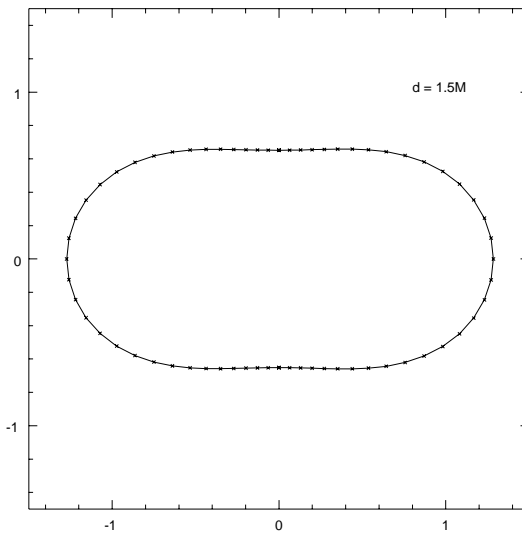


Figure 6.5: Separation of $1.5M$ with a 33^2 grid. The area is $185.41M^2$.

As we increase the separation between the two holes to a separation greater than the critical separation, we can test the apparent horizon tracker in the case of multiple apparent horizons. We demonstrate with a separation of $d = 2.0M$. The initial surface flows to the point of fissioning where the topology of the surface changes from a one surface into two surfaces. Fig. (6.7) is a plot of the initial surface that begins the flow. The level set found during this flow is depicted in fig. (6.8). Each of the surfaces in fig. (6.8) has a constant expansion, $\kappa = c_n$ and was used to indicate a topology change in the

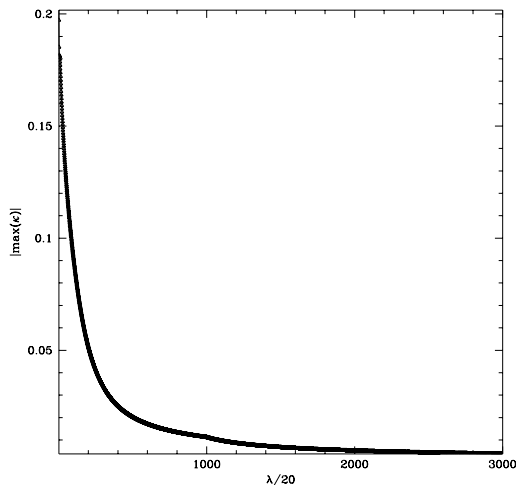


Figure 6.6: The absolute value of the maximum of expansion, κ , per iteration, λ every 20th step. The kinks at $\lambda = 1000$ and $\lambda = 2000$ are from restarting the code with a different λ -step.

test surface. The values for the expansion are $c_1 = 0.14$, $c_2 = 0.12$, $c_3 = 0.1$, and $c_4 = 0.08$. The last single surface just before the topology change is not a surface in the level set, it is plotted in fig. (6.9). At this point the tracker begins to flow two surfaces.

In contrast to a separation of $d = 1.5M$ where there is no fission, here as fissioning becomes imminent, the κ begins to increase. Fig (6.10) is a plot of the absolute value of the maximum across the surface of the expansion, κ , versus λ up to the point of fission. The increase in the expansion is one of the signals of imminent fission. As the algorithm tries to find a surface with $\kappa = 0$ everywhere, it is driven into two surfaces. Once the new surfaces are found, the maximum of the expansion begins a monotonic decrease as in fig. (6.6). The exaggerated peanut shape in fig. (6.12) and fig. (6.13) is taken at the same time as fig. (6.9).

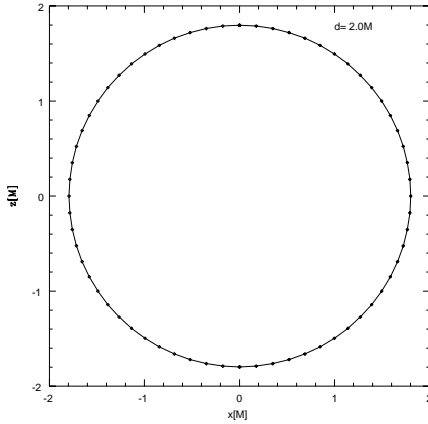


Figure 6.7: The starting surface of the level flow method for a separation of $d=2.0M$

Once the fissioning is detected by the code, it automatically begins flowing two new surfaces of the same resolution as the parent surface. The following series of snapshots is a subset of the set of surfaces found by the apparent horizon tracker as it follows the fission of the initial guess surface into two surfaces. The tracker starts with a spherical starting surface that deforms along the gradient field. As the points defining the surface flow, the distance between the points can become too small for the finite difference scheme at that resolution. Fig. (6.11) illustrates the difficulty of flowing the points of a surface. Redistribution of the points on the surface is taken care of automatically by updating the center and radius on the fly.

Once the level set of surfaces indicates a fission is occurring, a first guess at the two surfaces is made, and the two new surfaces are flowed. This is taken care of by estimating a new center and radius and flowing the new surfaces again. The final apparent horizons are known to $\epsilon_\kappa = 10^{-4}$.

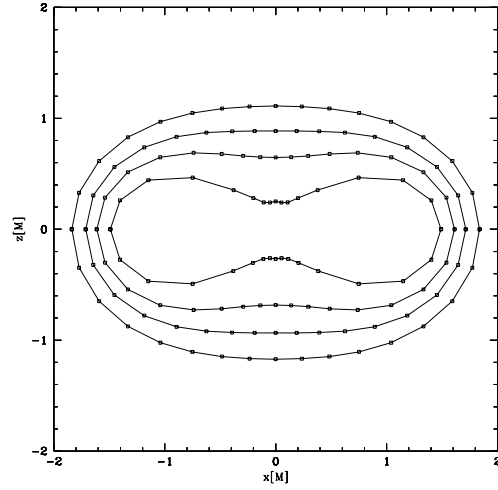


Figure 6.8: The level set of surface for the $d=2.0M$ case. Each surface has a constant $\kappa = c_n$ at each point. In this case the values for c_n are $c_1 = 0.14$, $c_2 = 0.12$, $c_3 = 0.1$, and $c_4 = 0.08$. The level set is used to indicate the change in topology associated with multiple surfaces.

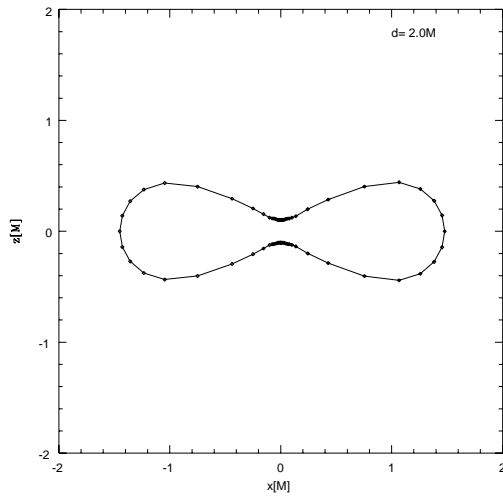


Figure 6.9: The single surface is about to fission into two surfaces.

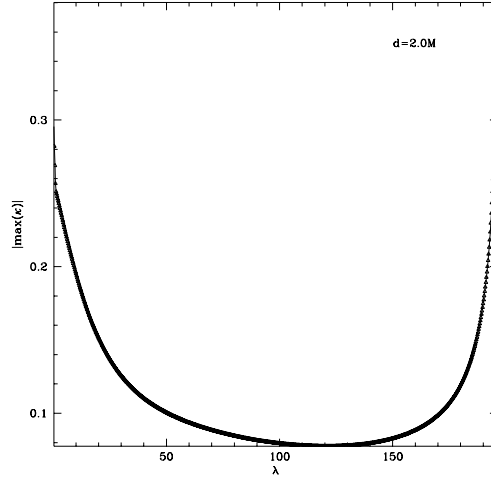


Figure 6.10: The absolute value of the maximum of expansion, κ , per iteration is plotted. The increase in the expansion is caused by imminent fission.

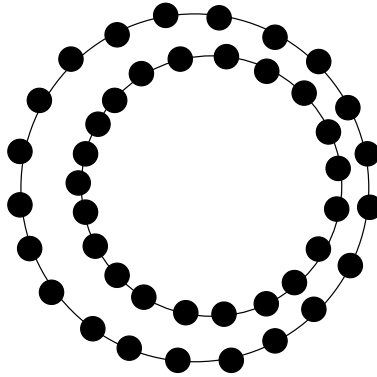


Figure 6.11: The surface is defined via the flow of its points. The points can “bunch” on the surface during flow. If the distance between points on the surface becomes too small, the iterative finite difference scheme fails to converge.

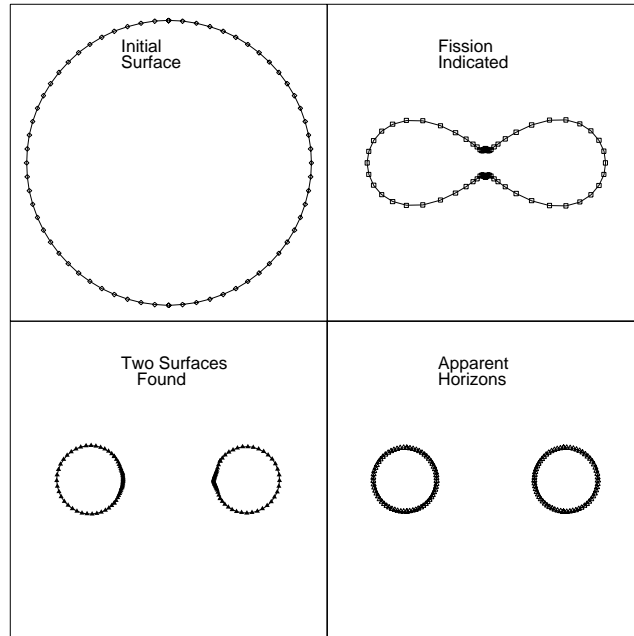


Figure 6.12: This series of snapshots depicts the flow of an initial surface until its fission for the binary Brill-Lindquist black holes separated by $2M$. The lower left plot is a first try at determining the final two surfaces. The cusps are due to a typical drawback associated with using points to define the flowing surface. The points crowd together in regions of greater flow. The next snapshot, on the lower right, shows the code's automatic correction; and shows the apparent horizons of the binary Brill-Lindquist data to an accuracy of 10^{-4} .

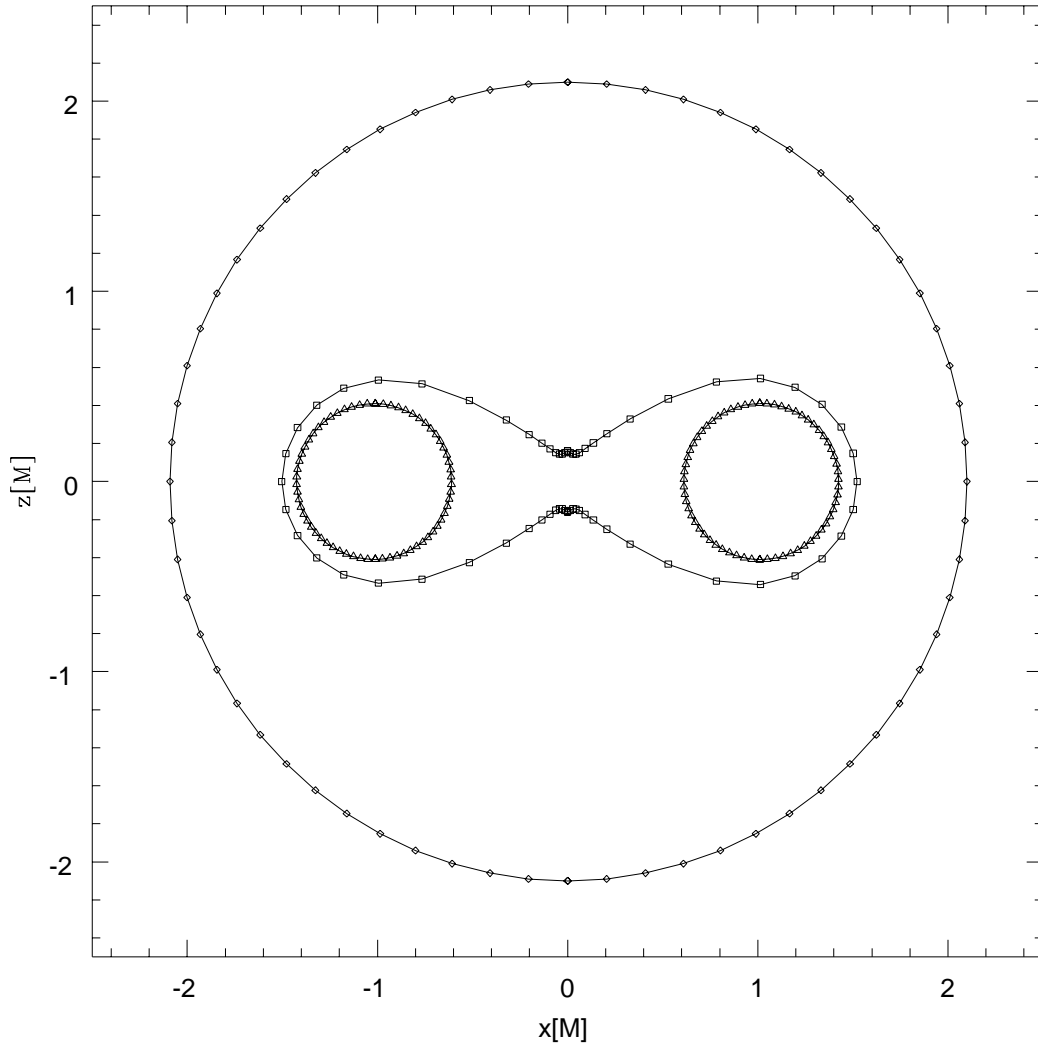


Figure 6.13: The series of pictures shown in fig. (6.12) are placed in one plot. The \diamond is the initial guess, the \square is the surface that is found indicating the need to search for two surfaces, and the \triangle is the results locating the apparent horizons for Brill-Lindquist data.

Chapter 7

Binary Black Hole Evolutions

In this chapter, I demonstrate the ability of the apparent horizon tracking code to locate multiple apparent horizons in a generic spacetime. I discuss the results of tracking the apparent horizons in a spacetime containing two colliding Kerr-Schild black holes. The spacetime is simulated with the evolution code developed by the National Science Foundation's Binary Black Hole Grand Challenge [7]. The initial data are the metric and extrinsic curvature of two superposed Kerr-Schild black holes [43], which were first evolved by Correll [24]. As I will explain further in § 7.3, the initial data implemented is an approximation to the complete initial data set with $\sim 10\%$ error in the constraint equations. The complete initial data set is under development at The Pennsylvania State University [16]; however, the approximate data set suits our purpose of demonstrating the apparent horizon tracker.

7.1 Kerr-Schild Metric

We chose a Kerr-Schild metric [45] for two reasons: 1) The metric is well defined at the event horizon, and 2) The metric is Lorentz form-invariant in a simple sense, under boosts ($v > 0$). The Kerr-Schild metric describes both the Schwarzschild and Kerr solutions to the Einstein equation. Eqn. (6.1) gives the metric; eqn. (6.12) gives the scalar function, and eqn. (6.13) gives the null vector.

The Kerr-Schild metric is cast into the 3+1 form in Cartesian coordinates by comparison with the standard 3+1 form of the metric:

$$ds^2 = -\alpha^2 dt^2 + \gamma_{ij}(dx^i + \beta^i dt)(dx^j + \beta^j dt). \quad (7.1)$$

The following definitions are the 3-metric γ_{ij} , the lapse function α , and the shift vector $\beta_i = \gamma_{ij}\beta^j$:

$$\gamma_{ij} = \eta_{ij} + 2Hl_i l_j, \quad (7.2)$$

$$\alpha = \frac{1}{\sqrt{1 + 2Hl_i^2}}, \text{ and} \quad (7.3)$$

$$\beta_i = 2Hl_i l_i. \quad (7.4)$$

The relation between the lapse and shift dictates that the horizon stays at a constant coordinate location in a nonboosted Kerr-Schild solution. The 3+1 split of the Kerr-Schild metric results in a 3-metric that depends on l_i and H as functions of (t, x, y, z) and an extrinsic curvature that depends on the following functions of (t, x, y, z) : l_i , $\partial_i l_\nu$, H , and $\partial_k H$.

7.2 Boosted Kerr-Schild Metric

The Kerr-Schild metric is form-invariant under a Lorentz transformation applied in a straightforward way: the Minkowski background, the scalar H , and the null vector, l_μ , are transformed as Lorentz objects; and the metric is recast. This is entirely equivalent to doing a coordinate transformation on $g_{\mu\nu}$ that coincides with the coordinate transformation implied by the Lorentz boost given in eqns. (7.5)-(7.7). Let a single black hole exist in a rest frame, $\bar{\mathcal{O}}$, with coordinates $(\bar{t}, \bar{x}, \bar{y}, \bar{z})$. Let \mathcal{O} be another frame with coordinates (t, x, y, z) . Frame $\bar{\mathcal{O}}$ is boosted relative to frame \mathcal{O} via $\hat{v}_i = (\hat{v}_x, \hat{v}_y, \hat{v}_z)$ with a speed, v , using the following transformation in which the black hole is moving with speed v in direction \hat{v}_i in the \mathcal{O} frame:

$$\Lambda_{\bar{t}}^{\bar{t}} = \gamma \quad (7.5)$$

$$\Lambda_{\bar{i}}^{\bar{t}} = -v\gamma\hat{v}_i \quad (7.6)$$

$$\Lambda_{\bar{j}}^{\bar{i}} = (\gamma - 1)\hat{v}_i\hat{v}_j + \delta_{ij}, \quad (7.7)$$

with $\delta_{ij}\hat{v}^i\hat{v}^j = 1$ and $\gamma = 1/\sqrt{1-v^2}$. With this transformation, a new null vector l_μ and a new function H are determined:

$$l_\mu = \Lambda_{\mu}^{\bar{\nu}}\bar{l}_{\bar{\nu}} \quad (7.8)$$

$$H = \bar{H}(\Lambda_{\mu}^{\bar{\nu}}\bar{x}_{\bar{\nu}}). \quad (7.9)$$

The form of the spacetime metric and its 3+1 decomposition remains unchanged in terms of l_μ and H .

To give a specific example, consider the Eddington-Finkelstein form of the metric, eqn (6.1). Let frame $\bar{\mathcal{O}}$ move relative to \mathcal{O} with a velocity, v , in the x -direction. The coordinates of \mathcal{O} are related to the coordinates of $\bar{\mathcal{O}}$ via

$$\bar{t} = \gamma(t - vx), \quad (7.10)$$

$$\bar{x} = \gamma(x - vt), \quad (7.11)$$

$$\bar{y} = y, \quad (7.12)$$

$$\bar{z} = z, \quad (7.13)$$

where v is the boost velocity and $\gamma = 1/\sqrt{1 - v^2}$ with $c = 1$. The coordinate transform between frames \mathcal{O} and $\bar{\mathcal{O}}$ is

$$\Lambda_{\bar{\mu}}^{\bar{\alpha}} = \frac{\partial \bar{x}^{\bar{\alpha}}}{\partial x^{\mu}}. \quad (7.14)$$

After the boost, l_i becomes

$$l_i = \partial_i(M/H) - \gamma v_i. \quad (7.15)$$

Since H is a scalar, it is invariant under this transformation. (The transformation changes only the coordinate labels of its argument point). The null vector and scalar function become explicitly:

$$r^2 = \gamma^2(x - vt)^2 + y^2 + z^2 \quad (7.16)$$

$$l_t = \gamma(1 - v\gamma(x - vt)/r) \quad (7.17)$$

$$l_x = \gamma(\gamma(x - vt)/r - v) \quad (7.18)$$

$$l_y = y/r \quad (7.19)$$

$$l_z = z/r \quad (7.20)$$

$$H = M/r. \quad (7.21)$$

The metric in the \mathcal{O} frame is given by:

$$g_{\mu\nu} = \Lambda_{\mu}^{\bar{\alpha}} \Lambda_{\nu}^{\bar{\beta}} g_{\bar{\alpha}\bar{\beta}}. \quad (7.22)$$

The lapse function and shift vector are defined as in eqn. (7.3) and eqn. (7.4). In fact, we have plotted the shift vector and lapse function for this boosted

Eddington-Finkelstein case in fig. (7.1). Fig. (7.1) shows a slice through the Eddington-Finkelstein in the xz -plane of a single black hole moving up the page with a velocity $0.5c$. Contours of constant α are depicted as cardioids and the inner ellipse is the horizon. The line segments indicate the magnitude of β_i and are directed out of the horizon. Note that the shift vector has a magnitude greatest in the wake formed as the black hole moves up the page.

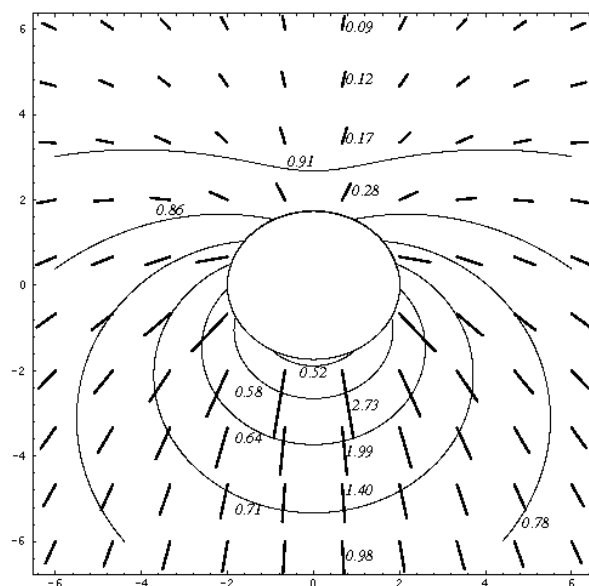


Figure 7.1: Contours of constant α are plotted as cardioids. The ellipse is the apparent horizon, which coincides with the event horizon. The shift vectors indicated by the line segments are directed away from the horizon and are greatest in the wake of the black hole as it moves up the page. This plot was generated using Mathematica for the Eddington-Finkelstein form of the Kerr-Schild metric. Coordinate labels are in units of M .

7.3 Initial Data

An isolated Kerr-Schild black hole has the metric:

$$\gamma_{ij} = \eta_{ij} + 2Hl_i l_j. \quad (7.23)$$

Approximate data for two Kerr-Schild black holes is constructed by superposing two isolated black hole metrics [24]. The resulting metric is

$$\hat{\gamma}_{ij} = {}_{(1)}\gamma_{ij} + {}_{(2)}\gamma_{ij} - \eta_{ij} \quad (7.24)$$

with the $\hat{}$ symbol indicating a quantity conformally related to the physical metric, $\gamma_{ij} = \phi^4 \hat{\gamma}_{ij}$.

$${}_{(1)}\gamma_{ij} = \eta_{ij} + {}_{(1)}H(r_1){}_{(1)}l_i{}_{(1)}l_j \quad \text{and} \quad (7.25)$$

$${}_{(2)}\gamma_{ij} = \eta_{ij} + {}_{(2)}H(r_2){}_{(2)}l_i{}_{(2)}l_j \quad (7.26)$$

are the the isolated Kerr-Schild metric forms with l_i and H corresponding to the single black holes. The two holes have comparable masses, $M_1 \sim M_2$, coordinate separation r_{12} , and velocities v_1 and v_2 assigned to them. For the argument of H and l_j , we use

$$r_1^2 = (x - x_1)^i (x - x_1)^j \delta_{ij} \quad \text{and} \quad (7.27)$$

$$r_2^2 = (x - x_2)^i (x - x_2)^j \delta_{ij} \quad (7.28)$$

with x_1^i and x_2^j the coordinate positions of the holes on the initial slice.

Following Matzner, Huq, and Shoemaker [43], the extrinsic curvatures of the two isolated black holes are added to obtain a trial \hat{K}_g^a for the binary black hole system given as:

$${}_{(0)}\hat{K}_j^i = {}_{(1)}\hat{K}_j^i + {}_{(2)}\hat{K}_j^i. \quad (7.29)$$

The subscript 0 indicates that this is an approximation to the true extrinsic curvature of the binary black hole spacetime. ${}_{(1)}\hat{K}_j^i$ and ${}_{(2)}\hat{K}_j^i$ are the individual extrinsic curvatures associated with the isolated Kerr-Schild metric and their indices are raised and lowered by their individual metrics, eqn. (7.23). Matzner *et al.* then follow the York prescription for initial data, separating the trace part of the extrinsic curvature, $K = \hat{K}(1) + \hat{K}(2)$; from the traceless part of ${}_{(0)}\hat{K}_{ab}$:

$${}_{(0)}\hat{K}_{ab} = {}_{(0)}E^{ab} + \frac{1}{3}\hat{\gamma}_{ab}K \quad (7.30)$$

$${}_{(0)}E^{ab} = \phi^{-10}({}_{(0)}\hat{E}^{ab}). \quad (7.31)$$

Note that the hatless quantity, ${}_{(0)}E^{ab}$, is the traceless part of the zeroth guess extrinsic curvature associated with the physical metric g_{ab} . A first attempt at writing the momentum constraint leads to

$$D_b({}_{(0)}E_c^b) - \frac{2}{3}D_c K \neq 0. \quad (7.32)$$

However, there is a violation of the momentum constraint due to the connections (Christoffel symbols) from hole(1) multiplied by the extrinsic curvature of hole(2) and vice versa

$$({}_{(1)}K^{ab})({}_{(2)}\Gamma^c{}_{db}) + ({}_{(2)}K^{ab})({}_{(1)}\Gamma^c{}_{db}) \quad (7.33)$$

(and similar terms) not predicted by eqn. (7.29) (where $\Gamma^c{}_{ab} = \frac{1}{2}\gamma^{cd}(\gamma_{da,b} + \gamma_{db,a} - \gamma_{ab,d})$ and ∂_c denotes a partial derivative). To determine the correct binary black hole constraints, a longitudinally contributing term is added to the traceless part of the extrinsic curvature. The new traceless part of the extrinsic curvature becomes:

$$A^{cb} \equiv {}_{(0)}E^{cb} + (lw)^{cb}, \quad (7.34)$$

where w^a is an undetermined vector and $(lw)^{cb}$ is the longitudinal addition given as:

$$(lw)^{cb} = D^c w^b + D^b w^c - \frac{2}{3} \gamma^{bc} D_d w^d. \quad (7.35)$$

Matzner *et al.* demand the solution of the momentum constraint, which in terms of the traceless and trace of parts of the extrinsic curvature is

$$D_b A^{cb} - \frac{2}{3} D^c K = 0, \text{ or} \quad (7.36)$$

$$D_b (lw)^{cb} = \frac{2}{3} D^c K - D_b ({}_{(0)}E^{cb}). \quad (7.37)$$

This is an elliptic equation for w^a . Using the following due to York [63]

$$D_b A^{cb} = \phi^{-10} \hat{D}_b \hat{A}^{cb}, \quad (7.38)$$

the momentum constraint can be written as:

$$\hat{D}_b (\hat{l}w)^{cb} = \frac{2}{3} \hat{D}^c K - \hat{\gamma}^{cb} \phi^6 \hat{D}_b ({}_{(0)}\hat{E}^{cb}). \quad (7.39)$$

Now w^a can be determined up to the function ϕ which is as yet undetermined. In order to obtain w^a and ϕ , the momentum and Hamiltonian constraints must be solved simultaneously. The Hamiltonian constraint following York's development is

$$8\hat{\Delta}\phi - \hat{R}\phi - \frac{2}{3}K^2\phi^5 + \phi^{-7}({}_{(0)}\hat{E}_{ij} + (\hat{l}w)_{ij})({}_{(0)}\hat{E}^{ij} + (\hat{l}w)^{ij}) = 0, \quad (7.40)$$

where $R = \hat{R}\phi^{-4} - 8\phi^{-5}\hat{\Delta}\phi$ was used. The solution to the coupled set of equations, eqn. (7.39) and eqn. (7.40), for w^a and ϕ constitutes a solution to the constraint equation. This involves solving the coupled elliptic equations eqn. (7.36) and eqn. (7.37).

A program to produce such solutions is being carried out by the group at the Pennsylvania State University [16]. The evolutions presented in this

dissertation have the initial data constructed from the zeroth guess extrinsic curvature, eqn. (7.29), and the superimposed metric, eqn. (7.24). The data describes two Kerr-Schild black holes initially separated by a coordinate distance exceeding $10M$ where M is the mass of one of the holes. The data violates the initial value equations by an error on the order $O(M/r)$, approximately 10% for black holes separated by $10M$. We find this an acceptable error considering the resolution of the run I include in this dissertation, which is 81^3 and a discretization size of $h = 0.25M$. We monitor the relative errors in the Hamiltonian and momentum constraints during the subsequent evolution, and find them to be small, of order 15% – 30%.

7.4 Binary Black Hole Evolution

The specific initial setup we implement is of two black holes of equal mass, M , both with initial spins in the positive z -direction, $a = 0.5M\hat{z}$, boosted towards each other in the x -direction with an initial velocity, $v = 0.5\hat{x}$. The black holes are a coordinate distance $10M$ apart in the x -direction and $2M$ apart in the y -direction at coordinate positions (x, y, z) $(-5M, -1M, 0M)$ and $(5M, 1M, 0M)$ on a Cartesian grid at the initial time, $t = 0$. The evolution is by a standard Cauchy code (a $\dot{\gamma}_{ij}$ and \dot{K}_{ij} code) which uses black hole excision. The evolution has 81^3 points distributed over the grid with a discretization size of $h=0.25M$. The domain is $\pm 10M$ in all directions. The computational evolution uses iterative Crank-Nicholson and singularity excision.

The excision masks are initially centered on the black holes. In a full implementation, the code would follow the apparent horizons by locating the apparent horizons on each time step, and revising the excision masks based on

the apparent horizon location(s). Here I am concerned with the behavior of the location of the apparent horizon in the evolving spacetimes, and with the understanding of the behavior of the evolution code for different treatments of the apparent horizon location. In the first instance I use an extrapolated estimate of the mask locations based on the known location at the initial configuration. Figure (7.2) plots the location of the two masked regions on the initial time slice.

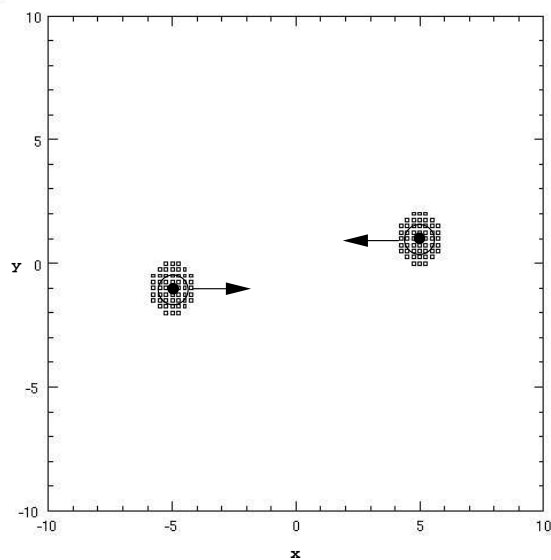


Figure 7.2: The data setup at $t=0$ contains a black hole at $(-5M, -1M, 0M)$ with $\vec{v} = (0.5, 0, 0)$ and a second black hole at $(5M, 1M, 0M)$ with $\vec{v} = (-0.5, 0, 0)$ as indicated by the arrows. Both holes have angular momentum about their axes, $\vec{a} = (0, 0, 0.5M)$ indicated by the symbol \odot .

We use the following lapse function and shift vector from the start of the evolution until the two black holes merge (the post-merger lapse and shift are defined later in the text)

$$\alpha_D = {}_{(1)}\alpha + {}_{(2)}\alpha - 1 \quad \text{and} \quad (7.41)$$

$$\beta_D^i = {}_{(1)}\beta^i + {}_{(2)}\beta^i; \quad (7.42)$$

where

$${}_{(1)}\alpha = \frac{1}{\sqrt{1 + 2{}_{(1)}H_{(1)}l_t}} \quad \text{and} \quad (7.43)$$

$${}_{(1)}\beta_i = 2H_{(1)}l_{t(1)}l_i, \quad (7.44)$$

and likewise for ${}_{(2)}\alpha$ and ${}_{(2)}\beta^i$ corresponding to the second black hole. This superposition of the isolated black holes' lapse and shift is not at all sophisticated, and better choices [43] may lead to significantly longer evolutions. Here, this choice appears acceptable. Our future evolutions will investigate better choices for the lapse and shift. Figure (7.3) depicts the contours of constant lapse values and the shift vectors for two Eddington-Finkelstein ($a = 0$) black holes superposed in the manner described above. The shift vectors behave in a similar manner to that of the single boosted black hole in fig. (7.1). The upper hole has a speed of $0.5c$ directed straight down the page and the lower hole has a speed of $0.5c$ directed up the page.

Eqn. (7.41) and eqn. (7.42) for the lapse and shift are used until the two single black holes approach close enough to be enclosed in a single apparent horizon. At that time, a weight function is used to gradually alter the lapse and shift to accommodate the new single black hole. The new lapse function is

$$\alpha_S = \frac{1}{\sqrt{1 + 2M_S/r_S}}, \quad (7.45)$$

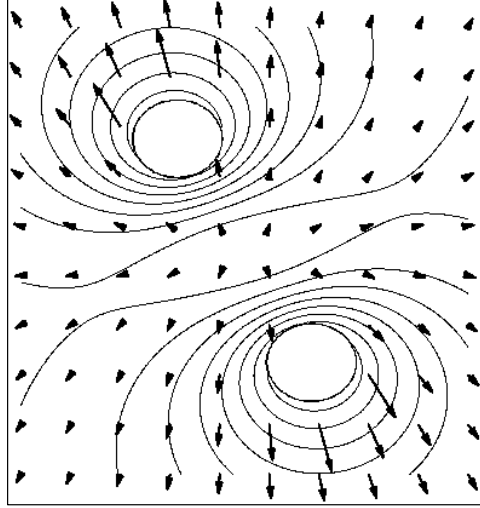


Figure 7.3: Two Eddington-Finkelstein ($a = 0$) black holes showing contours of constant lapse. The upper hole has a speed of $0.5c$ directed straight down the page and the lower hole has a speed of $0.5c$ directed up the page. The arrows show the magnitude and direction of the shift vector.

and the shift vector is

$$\beta_{iS} = \frac{2M_S x_i}{r_S r_S}, \quad (7.46)$$

where $M_S = M_1 + M_2$ and $r_S = \sqrt{x^2 + y^2 + z^2}$. For the post-merger results given in this dissertation, we used a lapse and shift each defined in terms of a mass $M_S/2$. This may have contributed to shortening the length of the post-merger evolution achieved. We are carrying out further evolutions with post-merger lapse and shift as in eqns. (7.45) and (7.46). At any rate, there is no affect on the apparent horizon tracking. The intermediate lapse function and shift vector, while they are being blended with a weight function, are

$$\alpha = (1 - W)\alpha_D + W\alpha_S \quad \text{and} \quad (7.47)$$

$$\beta^i = (1 - W)\beta_D^i + W\beta_S^i \quad (7.48)$$

respectively. The weight function effecting the change is

$$W = 1 - 3 \left(\frac{t - t_F}{t_I - t_F} \right)^2 + 2 \left(\frac{t - t_F}{t_I - t_F} \right)^3 \quad (7.49)$$

where $t < t_I \Rightarrow W = 0$ corresponding to $\alpha = \alpha_D$ and $t > t_F \Rightarrow W = 1$, corresponding to $\alpha = \alpha_S$ and similarly for β_i . The time t_I is the time when a single spherical mask of radius $4M$ will fit inside the single apparent horizon enclosing both black holes and the time t_F was chosen to allow a gradual transition.

In a numerical Cauchy simulation of a spacetime, outer boundaries must be placed at an arbitrary, finite distance rather than at the physically appropriate infinity. Conditions are placed at these outer boundaries that approximate the behavior of the region stretching to infinity. However, errors are inevitable except in very simple situations. The grazing collision of two black holes is not a simple situation, so we work to minimize the errors with the least amount of effort. The outer boundary condition chosen for this evolution is a blended Dirichlet condition [30], a means of providing approximate analytic data at the boundaries. We solve the initial data problem at the boundaries at each time step. For the run described here, the Dirichlet data specified at the boundaries is for two black holes even after the holes merge. We are presently modifying the algorithm for the outer boundary to one in which a transition between the double and single hole occurs also in the approximate boundary condition. A smooth transition between the numerical interior data and the analytic boundary data is implemented by blending through a few spatial points near the boundary. The geometry of the blending is based on the cubical computational domain faces. Future evolutions will be done with a

spherical blending geometry. The spherical geometry is more closely adapted to the topology of the outgoing gravitational waves generated in the encounter than is the cubical; and has been seen in experiments to generate fewer errors at the boundary than does the cubic blending.

The inner boundary associated with avoiding computations near the singularities of the black holes was discussed in Chapter 1. We discussed that the evolution code currently implements a masking technique to remove the singularities based on the estimated locations of the apparent horizons at each instant of time. For the first simulation described here, the location of the apparent horizons for the two black holes is estimated based on Lorentz transformations from the initial of position of each isolated black hole. This guess determines the masked region. But this works only so long as the guess is close to the true location of the apparent horizon. If the mask falls outside of the true apparent horizon location, the evolution will fail.

In carrying out a simulation with this extrapolated location for the masks, failure does occur, apparently due to incorrect prediction of the location of the horizons at time approximately $3.5M$, where M is the mass of each black hole. Fig. (7.4) is a plot of the component g_{xx} with $x = z = 0$ versus y and time. This plot “misses” the masks; however fig. (7.5) is plot of g_{xx} with $y = z = 0$ along the x -axis as a function of time and show the two masks. The two masked regions in fig. (7.5), seen as two small flat regions at $\pm 5M$ at $t = 0M$ with an increasing amplitude in g_{xx} near the masks. The amplitude is at a maximum at the last recorded time of the run. Fig. (7.6) is a plot of the normalized Hamiltonian constraint along the y -axis ($x = z = 0$) versus time. The normalized Hamiltonian constraint is designed to range between -1 to 1 by taking the Hamiltonian constraint and dividing it by the norm of

its components as given by:

$$\frac{HC}{|HC|} = \frac{K^2 - K_{ij}K^{ij} + R^2}{|K|^2 + |K_{ij}||K^{ij}| + |R|}, \quad (7.50)$$

where $|\dots|$ indicate that the absolute value of the component has been taken. The fig. (7.6) is of the same view as fig. (7.5) in that it gives the time history of the y -axis which does not intersect the masks. Fig. (7.7) also plots the variation of the constraint but along the x -axis versus time with $y = z = 0$. This figure is a good diagnostic. We see spikes growing with time near the masks. These strong deviations from zero are errors in Hamiltonian constraint plausibly caused by the extrapolated mask locations not correctly masking the region inside the apparent horizon. As in fig. (7.5), the amplitude of the normalized Hamiltonian constraint has a maximum at the last time step. Fig. (7.8) and fig. (7.9) show sequences of plots of the metric function, g_{xx} , and the normalized constraint, $HC/|HC|$. These plots are in the xy -plane since the initial separation of the holes is in the xy -plane. The increasing spikes seen in Hamiltonian constraint are really inside of the apparent horizon. The growth of these errors eventually stops the evolution at $3.5M$. The increasing deviation from 0 of the normalized Hamiltonian constraint at the outer boundaries is a result of our choice of boundary conditions. Better outer boundary conditions are being researched.

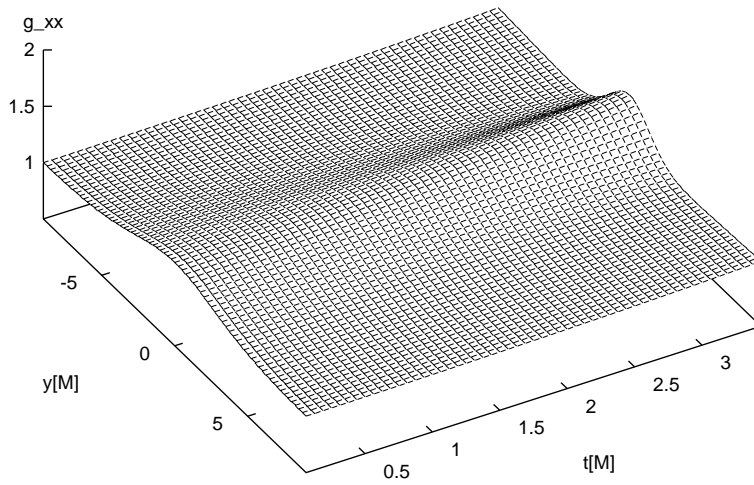


Figure 7.4: The metric component, g_{xx} , sliced at $x = z = 0$ and plotted versus y and t from $t = 0M$ to $t = 3.5M$. From this view, the masks cannot be seen.

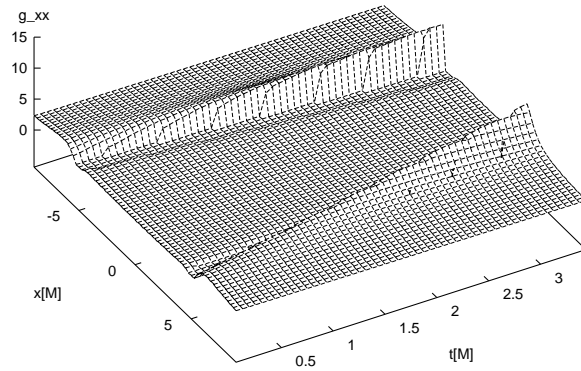


Figure 7.5: The metric component, g_{xx} , sliced at $y = z = 0$ is plotted versus x and t from times $t = 0M$ to $t = 3.5M$. The masked region can be seen at $-5M$ and $5M$ at $t = 0$ on the x -axis. g_{xx} is growing with time near the masks.

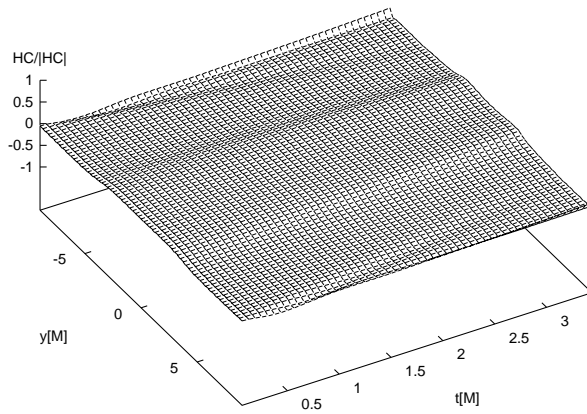


Figure 7.6: The normalized Hamiltonian constraint is sliced at $x = z = 0$ and plotted versus y from times $t = 0M$ to $t = 3.5M$. A small deviation from 0 is seen along the outer boundary.

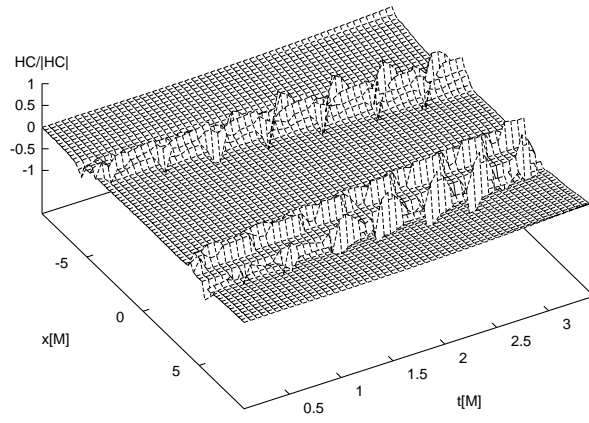
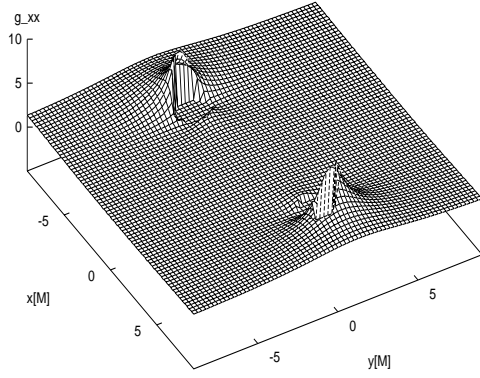
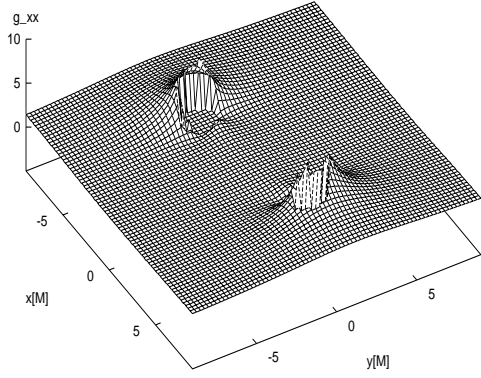


Figure 7.7: The normalized Hamiltonian constraint is sliced at $y = z = 0$ is plotted versus x and t from times $t = 0M$ to $t = 3.5M$. The error in the Hamiltonian constraint is growing with time around each masked region.

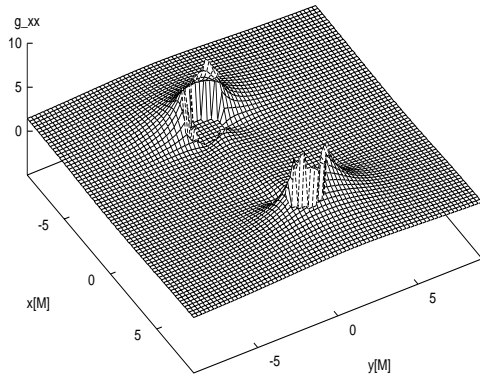
0.0M



1.7M



2.6M



3.4M

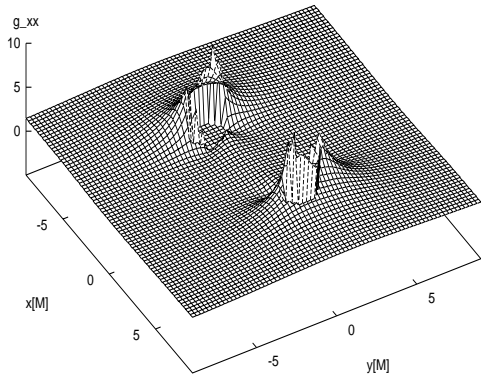
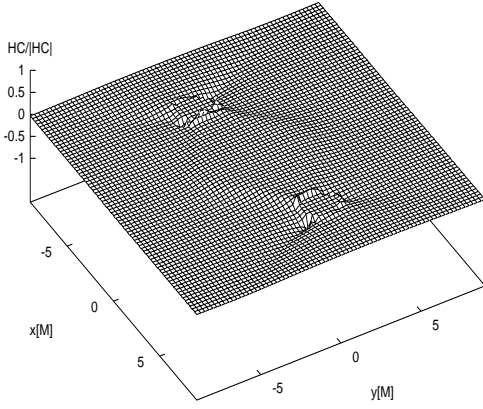
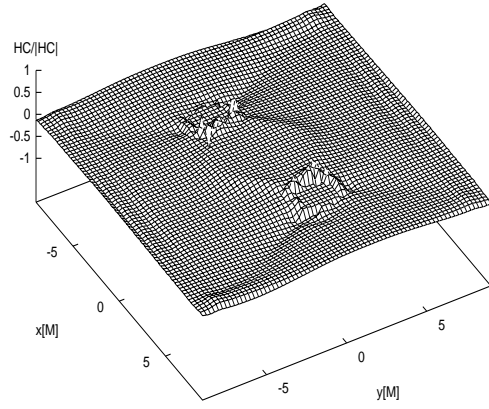


Figure 7.8: The metric component, g_{xx} , is sliced at $z=0$ and plotted through a sequence of times. The spikes increase with time, an indication that our masking procedure is failing.

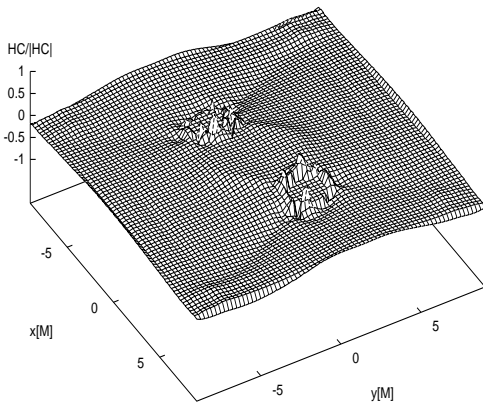
0.0M



1.7M



2.6M



3.4M

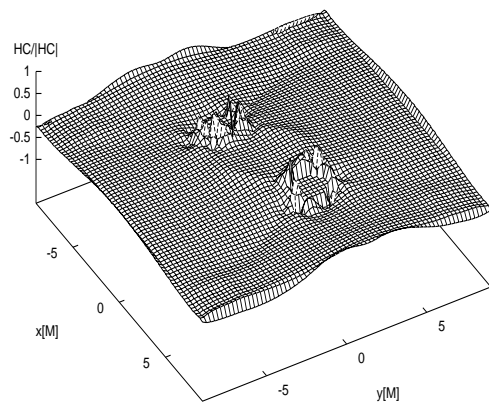


Figure 7.9: The normalized Hamiltonian constraint is sliced at $z=0$ and plotted through a series of times. The spikes in the data are interior to the apparent horizon.

7.5 Black Hole Evolution with Apparent Horizon Tracking

The previous evolution stopped at $3.4M$ with increasing errors in the normalized Hamiltonian constraint near the masked region. At the present time, the apparent horizon tracker is not automatic in the evolution code. With the computed metric and extrinsic curvature in hand, I locate the apparent horizons in the $3.4M$ computed spacetime using the level flow method described in Chapter 5 using $N^2 = 33^2$ points distributed on the 2-surface. I found two important pieces of information: 1) that the masks no longer are centered within the apparent horizon, and 2) that the apparent horizon at $3.4M$ enveloped both black holes. The first point means the masks lagged behind the true location of the apparent horizons. The mask location for moving black holes is determined by extrapolating the motion of the black hole linearly, the masks were given a constant velocity of $\pm(0.5c, 0, 0)$. However, the apparent horizon locations show that there is an effective acceleration of the horizons toward one another. This acceleration means that the black holes move faster in the x and y directions than the extrapolated motion of the masks. Thus the masks undershoot the positions of the horizons and the evolution fails since either the singularity is uncovered or the mask is outside of the apparent horizon, hiding parts of the spacetime in causal contact with the observer. We estimated the coordinate speed of the apparent horizons to be approximately $\pm(0.55c, 0.06c, 0)$.

The second point, that a single apparent horizon envelopes both black holes at $3.4M$, together with the increase in speed is a key to making the evolution continue past $3.4M$. By increasing the speed to $\pm(0.55c, 0.06c, 0)$,

we were able to keep the code running past the merger of the two black holes. We used the merger at $3.4M$ to predict when to change from two masks to a single mask. The mask geometry is spherical, so the two masks are kept until both singularities are predicted to be within a sphere of radius $4M$. From the apparent horizon locations at $t = 0M$ to $t = 3.4M$, we predicted that a single, spherical mask at $5M$ would be successful. The lapse function and shift vector were changed to eqn. (7.45) and eqn. (7.46) according to the weight function given in eqn. (7.49). I then use the apparent horizon tracker on the last few instants of this evolution. The tracker finds that there is a single apparent horizon enveloping the holes at $3.4M$. From $3.4M$ to $8.3M$ a single black hole, resulting from the merger to two black holes is evolved. The evolution has gone to merger!

The following plots are of the metric function g_{xx} and the normalized Hamiltonian constraints. They are plotted versus time from $0M$ to $8M$ to demonstrate what is happening as the two holes move together. Fig. (7.10) is the time dependence of the metric component sliced at $x = z = 0$ plotted versus y and t , and fig. (7.11) is sliced at $y = z = 0$ plotted versus x and t . Both figures show the masked region of the two holes merge into one mask at $5M$ based on the locations of the apparent horizons. Fig. (7.12) is the time dependence of the Hamiltonian constraint sliced at $x = z = 0$ and fig. (7.13) is sliced at $y = z = 0$. Notice that the errors in the normalized Hamiltonian constraint almost disappear as we merge into a single masked region although there is some error propagating in from the outer boundaries. In comparing fig. (7.10) to fig. (7.4), we see the masked region due to forming single hole clearly; however, comparing fig. (7.11) to fig. (7.5) is more more interesting. We see that the spikes along the masked regions decrease in fig. (7.11) as a

single mask is formed. Similarly, comparing fig. (7.13) and fig. (7.7) shows a decrease in amplitude in the spikes near the mask in fig. (7.13) as a single mask is formed.

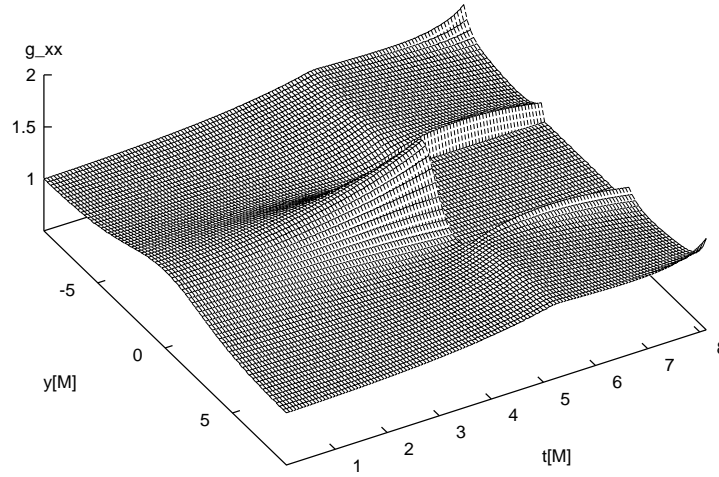


Figure 7.10: The metric component, g_{xx} , is sliced at $x = z = 0$ from times of 0M to 8M. This plot shows the time dependence on the numerical grid function. In contrast to fig. (7.4), g_{xx} decreases in time once a single mask is used.

Fig. (7.14) and fig. (7.15) are snapshots of the metric component and normalized Hamiltonian constraint at particular times during the evolution. These times correspond to the times we have located apparent horizons seen in fig. (7.19). All snapshots show $z = 0$ data. These figures show the movement of the two holes towards each other and their eventual merger. The deviation from 0 in the normalized Hamiltonian constraint, fig. (7.17) and fig. (7.15) is due to incorrect blending to the numeric solution at the boundary. The spikes in the corners are due to our choice of a cubical geometry in the blending region,

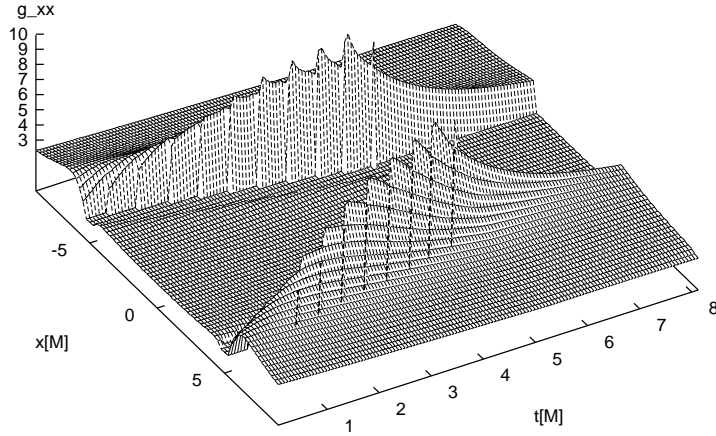


Figure 7.11: The metric component, g_{xx} , is sliced at $y = z = 0$ from times of $0M$ to $8M$. This plot shows the time dependence on the numerical grid function. In contrast to fig. (7.5), g_{xx} decreases in time once a single mask is used.

future runs will use spherical blending. Further errors arise because I do not switch to a single mask for at the outer boundary in this run, but continue to use two moving holes as data. Fig. (7.16) and fig. (7.17) show snapshots of the metric component and the normalized Hamiltonian constraint at the time before we choose a single mask, $5M$, the time after we have completed the single hole transition, $5.3M$, and the last reasonable time step of the evolution, $8.1M$, when we choose a single mask

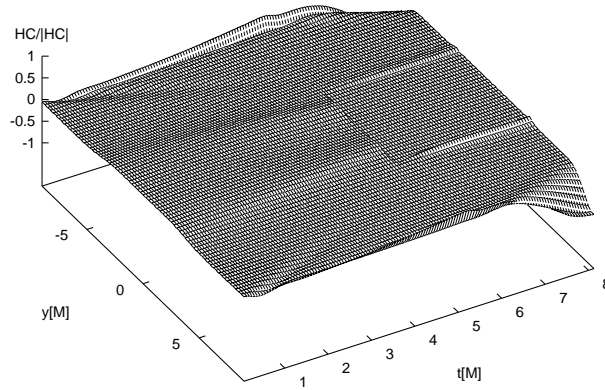


Figure 7.12: The normalized Hamiltonian constraint is sliced at $x = z = 0$ from times of $0M$ to $8M$. This time dependent plot also demonstrates the reduction of error as the single, merged mask is used.

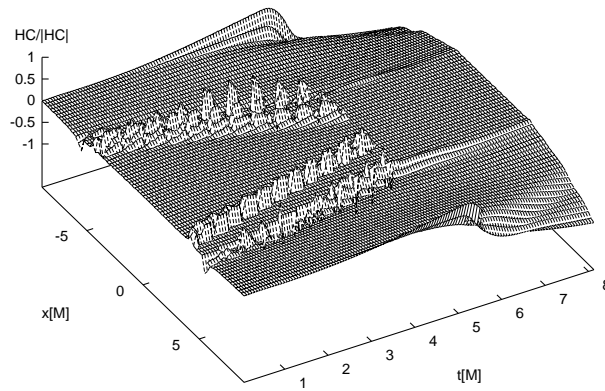
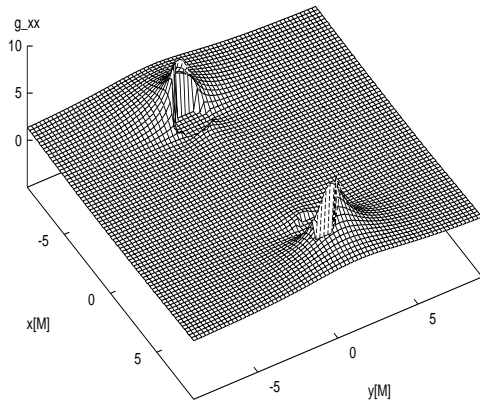
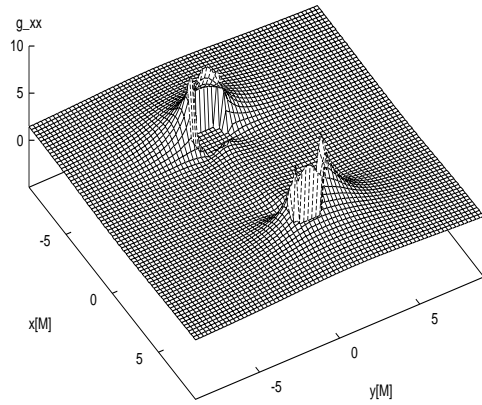


Figure 7.13: The normalized Hamiltonian constraint is sliced at $y = z = 0$ from times of $0M$ to $8M$. This time dependent plot also demonstrates the reduction of error as the single, merged mask is used.

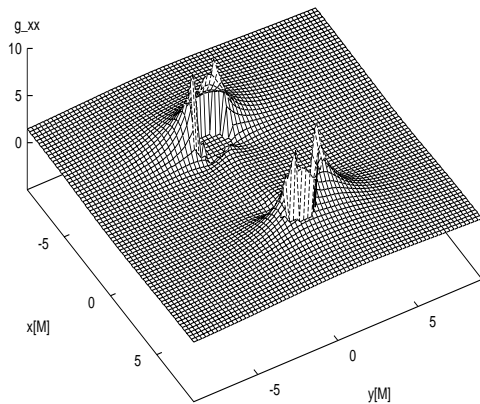
0.0M



2.8M



3.4M



7.8M

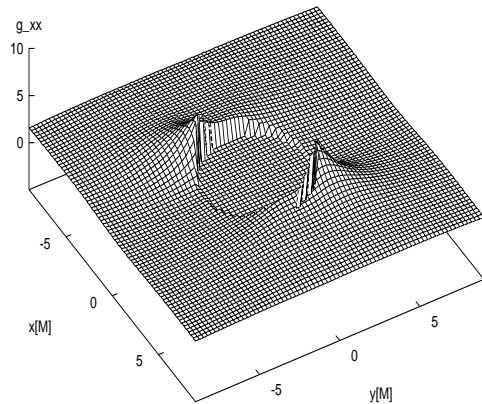


Figure 7.14: A time series of the metric component, g_{xx} , is sliced at $z = 0$. The spikes are greatly reduced from the previous evolution, fig. (7.8). The times associated with these snapshots are the same times as the apparent horizons shown in section 7.6.

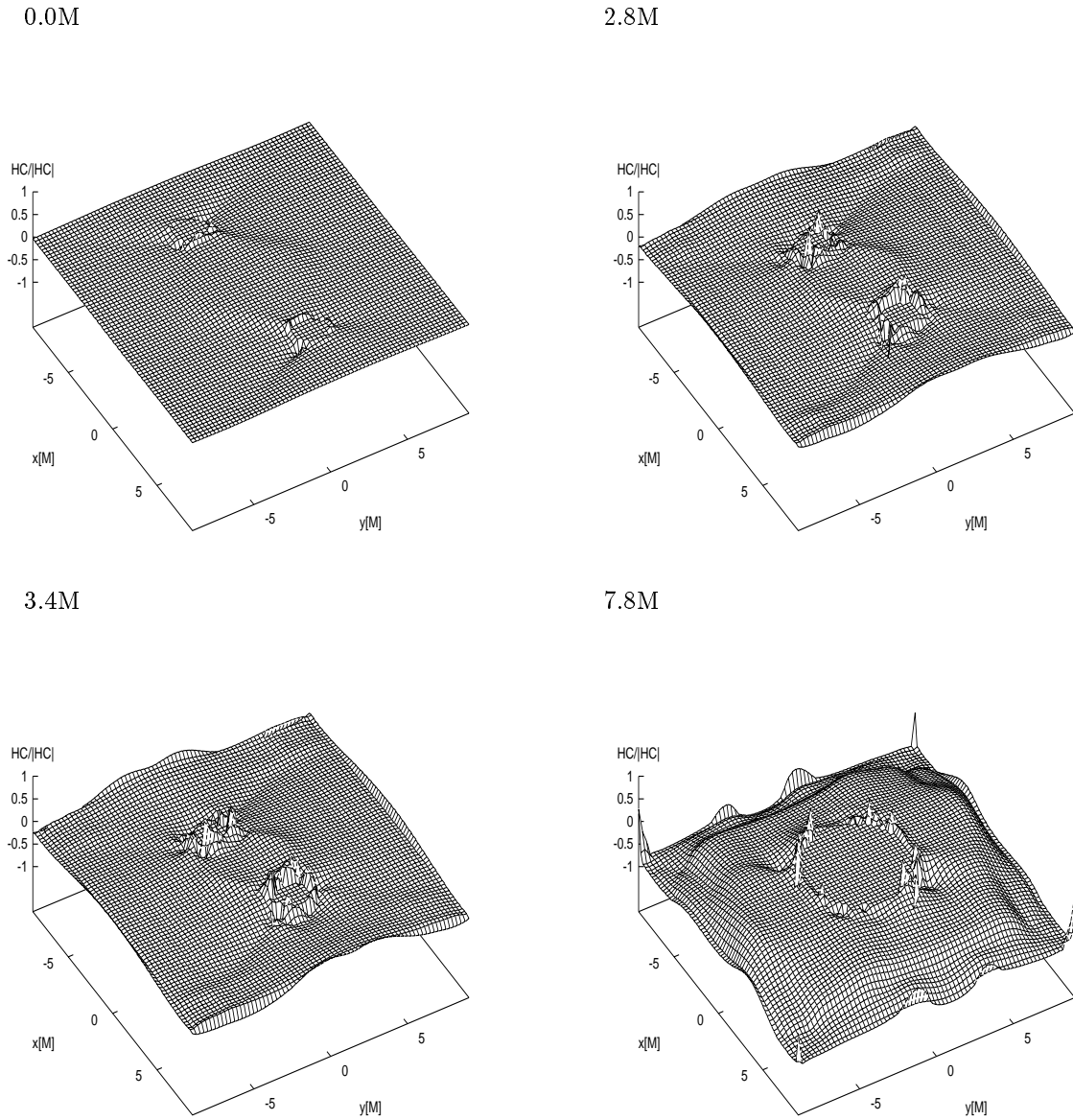
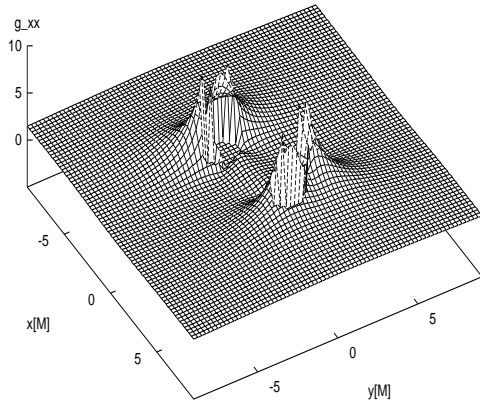
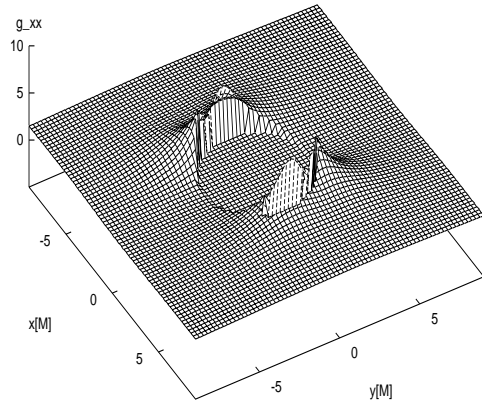


Figure 7.15: The normalized Hamiltonian constraint sliced at $z = 0$ and presented in a time series. These plots concur with the metric component. The errors are greatly reduced from the previous evolution, fig. (7.9). These snapshots correspond in time with the apparent horizons shown in section 7.6.

5.0M



5.3M



8.1M

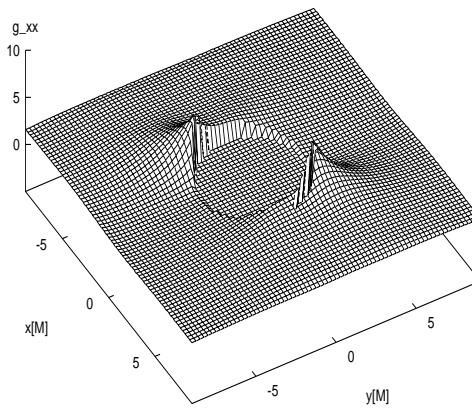
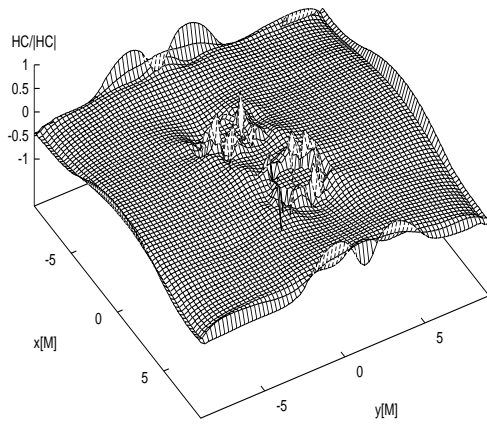
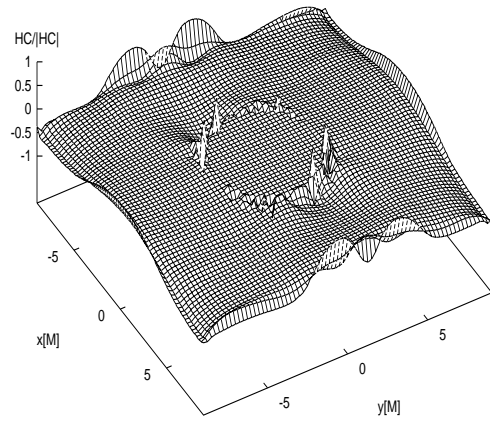


Figure 7.16: A time series of the metric component, g_{xx} , is sliced at $z = 0$. The spikes are greatly reduced from the previous evolution, fig. (7.8). The snapshots were taken at the times corresponding to the beginning and end of the weighted merger from a double masked region to a single masked region; and the final time of the evolution.

5.0M



5.3M



8.1M

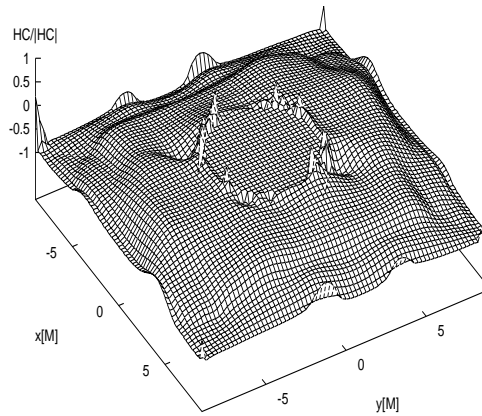


Figure 7.17: The normalized Hamiltonian constraint sliced at $z = 0$ and presented in a time series. These plots concur with the metric component. The errors are greatly reduced from the previous evolution, fig. (7.9). The snapshots are of the beginning and end of the merging of the masks plus the final time.

7.6 Apparent Horizons in the Binary Black Hole Merger

The apparent horizons are tracked using the level flow method discussed in Chapter 4. Fig. (7.18) shows the progression of the horizons through the evolution including the masked region used in the evolution code. As long as the masked region lies inside the apparent horizon, no information is lost. However, if the masked region is too small, the singularity may become uncovered. This is a problem when the black holes merge into a single apparent horizon but the two masks remain separate .

The apparent horizons obtained in $\Sigma(t = 0.0M)$, $\Sigma(t = 2.8M)$, $\Sigma(t = 3.4M)$, and $\Sigma(t = 7.8M)$ are plotted in fig. (7.19). Already at $2.8M$, the apparent horizons have deviated from their approximately spherical shape noticeable at $0M$. The effect of the holes on each other is in evidence. The dramatic change in the shape of the apparent horizon between times $3.4M$, the first time a single apparent horizon envelopes both black holes, and $7.8M$ is seen in fig. (7.20). This large change in shape suggests strong dynamics which could lead to strong radiation. There is also an apparent rotation of the horizon as the holes spin towards each other. We are working to extend the domain off the computation to allow extraction of the waveforms in this evolution and reconstruction of the event horizon. Runs with different black hole angular momentums, and angular momenta in different directions are being planned.

Our selection of apparent horizons are plotted in all three planes in fig. (7.21). The distortion of the holes as the move toward each other is seen, especially in the y axis. The apparent horizons of the holes shrink in the

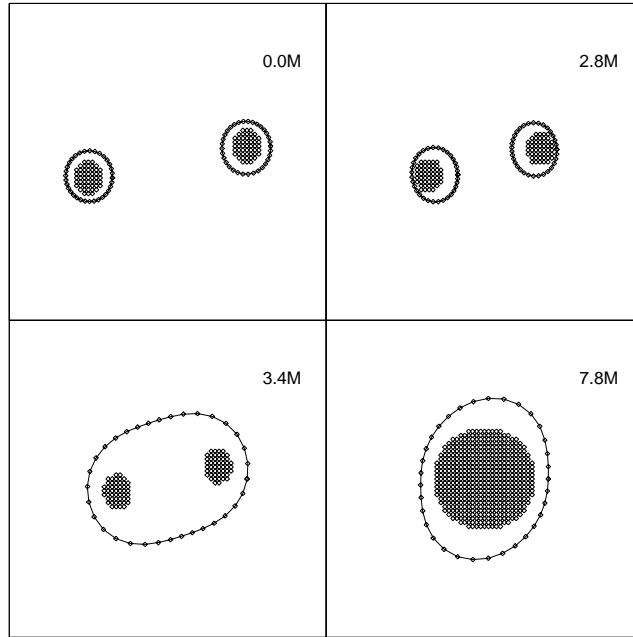


Figure 7.18: Snapshots of the apparent horizon(s) with the masks included. The mask for each black hole is the region represented as the diamonds in the interior of each apparent horizon. The axes are all y vs. x with a range of $[x_{min} : x_{max}] = [y_{min} : y_{max}] = [-10 : 10]$.

x -direction giving them a flattened appearance.

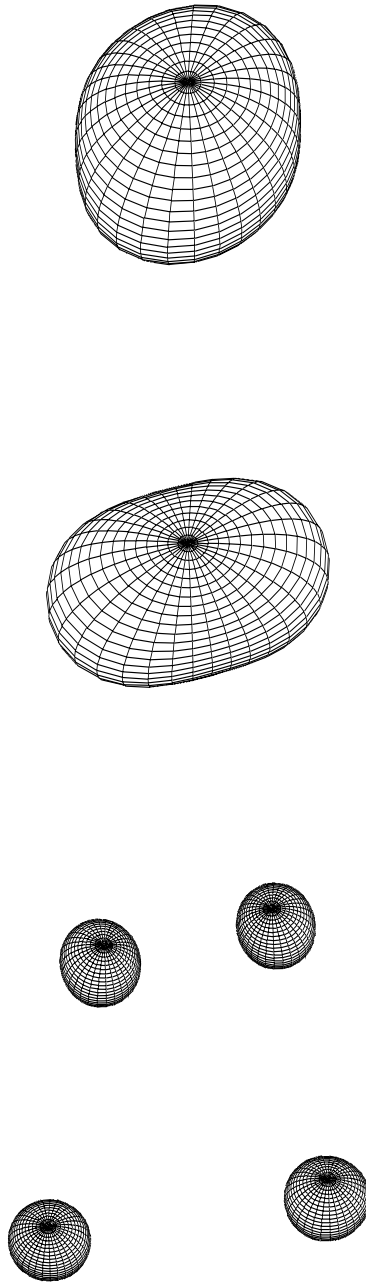


Figure 7.19: The apparent horizons are plotted up the page as a function of evolution time. The times are going up the page: $0M$, $2.8M$, $3.4M$, and $7.8M$.

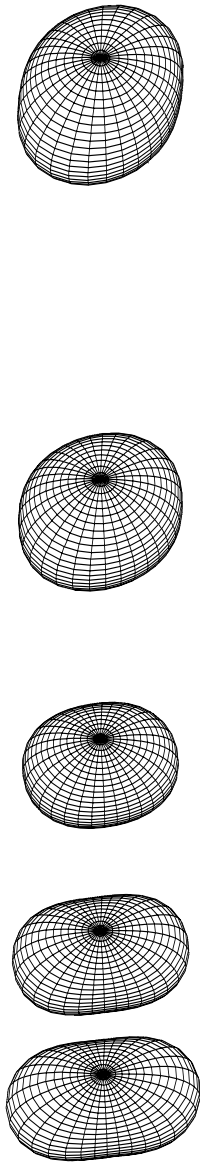


Figure 7.20: The apparent horizons are plotted up the page as a function of evolution time. These pictures are all after the merger. The times are going up the page: $3.4M$, $3.8M$, $4.6M$, $5.6M$, and $7.8M$. An apparent rotation in the horizon is seen from $3.4M$ to $7.8M$.

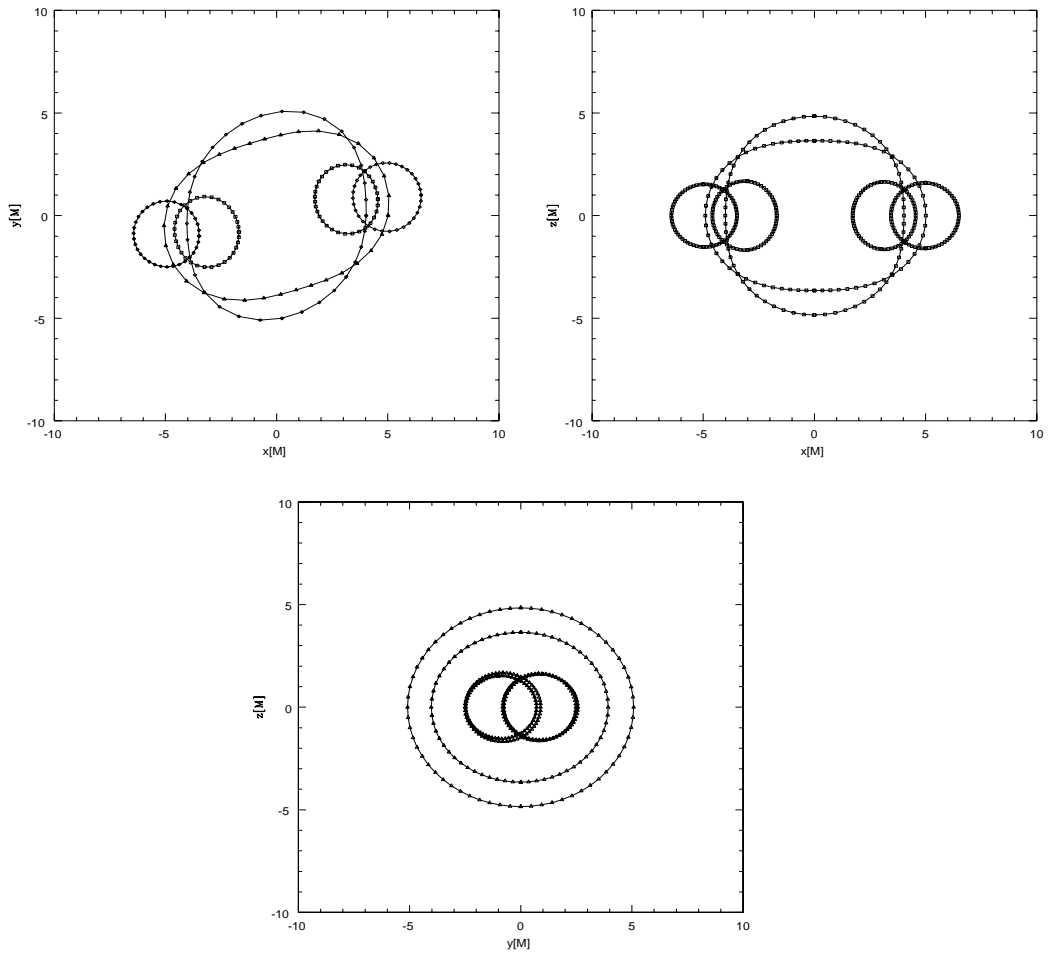


Figure 7.21: The apparent horizons are plotted in each plane on top of each other to illustrate the deformation of the horizons.

Until we have evolved the spacetime to quiescence and found the event horizon, the apparent horizon is the best indicator of the dynamics occurring in this problem. Although the above evolution is short, the most dramatic dynamics have occurred. At $3.4M$ the black holes merge and evolve another $4.4M$ as a single black hole. Referring to fig. (7.20), we see a rotation in the apparent horizon. At $3.4M$, the apparent horizon is thinner along the y -axis and fatter along the x -axis. This is expected since the holes are approaching each other with greatest speed along the x -axis. However, as the single hole evolves to $7.8M$, the horizon becomes shortened along the x -axis and elongated along the y -axis. This rotation results from the collision of two spinning black holes offset in the y and x axes. The internal angular momentum of each single black hole plus the orbital angular momentum of the single holes contribute to the angular momentum of the final spinning, single black hole. The final angular momentum per unit mass of the black hole is unknown; however, this simple addition implies the angular momentum per unit mass of the black hole approaches M . We cannot conclude how long the merged black hole will take to reach a static equilibrium, approaching a Kerr black hole with angular momentum without a longer evolution.

A second and related indicator of the dynamics is the change in the area of the apparent horizon during the evolution. A plot of the area is in fig. (7.22) with the areas of the apparent horizons at times prior to $3.4M$ added together. At the initial time step, the area is $43.6M^2$ for each black hole. At time $2.8M$, each hole has an area of $44.2M^2$; therefore, the area has remained basically unchanged during this early part of the evolution. Once the black holes merge, at $t = 3.4M$, the area increases to $184M^2$. Based on merging Schwarzschild hole simulations, the mass will approximately double; the radius will double

and the area will quadruple with very In this case we would expect an area of approximately $176M^2$ for the merged hole, so the merged black hole has an area exceeding expectations by about 5%, not a significant error considering the accuracy of the computation. As the evolution continues, the area of the apparent horizon continues to increase: at $t = 5.6M$ the area is $292M^2$ and at $t = 7.8M$ the area is $310M^2$. The increase in area indicates infall of radiation into the black hole. By the end of this evolution, the area has increased by a factor of 1.6. Considering the dynamics of the situation, we conjecture that a large amount of radiation is being produced and falling into the black hole. We also conjecture that the event horizon is considerably bigger than the apparent horizon at early times in the evolution. In the future, once the dynamics of the collision are played out, we will identify the event horizon.

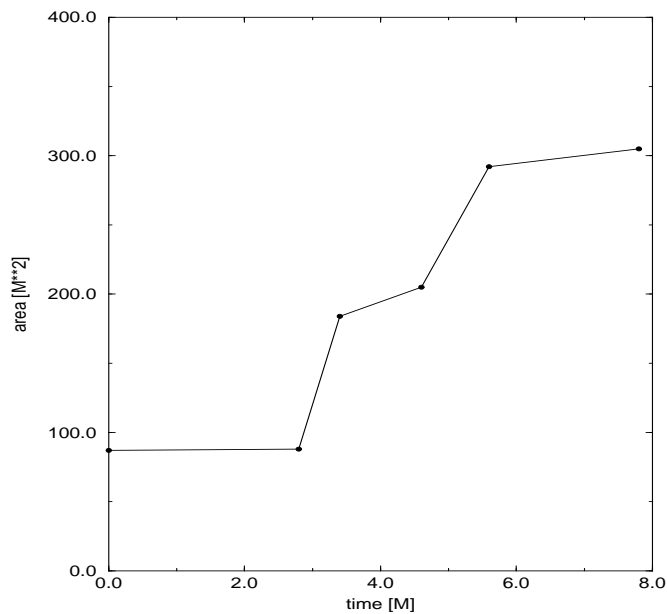


Figure 7.22: The numerically computed area of the apparent horizon versus time for the binary black hole grazing collision.

Chapter 8

Conclusions & Future Work

8.1 Significance of Results

There are two major results in this dissertation: 1) The development of a generic multi-black hole apparent horizon tracker, and 2) The use of apparent horizon tracking in the first grazing collision of binary black holes implementing excision. The purpose of the work on apparent horizon tracking was to create a code with the capability to detect multiple apparent horizons in generic spacetimes. We have shown the tracker at work in a situation of great importance to numerical relativists, the merger of two Kerr-Schild black holes. We saw the two horizons tracked from a single initial guess merge into a single apparent horizon during the simulation. A significant step towards building a laboratory to study strong field gravitation!

Other codes [44] with the capability to evolve a binary black hole spacetime to merger in a grazing collision do not use excision to mask the singularities, but rather “traditional” techniques of lapse choices that avoid the singu-

larities such as maximal slicing. These techniques do not excise the singularity region with apparent horizons, instead they avoid evolving the spacetime in the vicinity of the singularity by using a lapse that does not reach the singularity. This leads to problems at later times in the simulation due to large gradients in the coordinates near the singularity. These codes can run the collision longer than the excision method described here; however, they are at the limit of that technique. Longer evolutions are not possible with non-excision techniques despite increases in resolution.

The key to the success of the binary black hole merger presented here was better predictions of the locations of the apparent horizons and especially the knowledge of when a single apparent horizon envelops both black holes. This was the motivation behind designing an apparent horizon tracker capable of finding multiple apparent horizons. We listed a set of criteria for apparent horizon trackers that included: (1) The robustness of the tracker due to its lack of dependence on changes to the initial guess; (2) The generality of the tracker in its applicability to generic spacetimes including multiple black hole spacetimes; and (3) The efficiency of the tracker algorithm in CPU time. We have demonstrated the ability of the level flow method in criteria 1 and 2. Improvement with regard to the third criterion, however, is part of the future work.

8.2 Near-Future Work

The building of a theoretical laboratory for astrophysically relevant black hole interactions is a work in progress. This dissertation discussed the building of a single tool in the laboratory's toolbox. The apparent horizon tracker

eventually will be integrated into an evolution code. In this thesis we used the 3+1 evolution code developed by the NSF Computational Grand Challenge Alliance. We are in the process of integrating the tracker into the AGAVE code [1], a code based on the Grand Challenge Alliance code with infrastructure from the CACTUS [17] distribution.

The speed of the horizon tracker in its current implementation is poor. Although the tracker is comparable in speed to other trackers (fast flow [33]) at particular resolutions [5]; it is still the case that this code is approximately four times slower than the evolution for a particular size run, for example $81 \times 81 \times 81$. A major contributing factor to the slowness of the level flow code is the interpolation from the Cartesian grid where the metric and extrinsic curvature components are defined to the 2-surface. Since the apparent horizon locations are not needed at every time step, the tracker not be run at every time step; therefore, the speed of the method is not a top priority. However work to increase the speed of the tracker is in progress. I have created a To-Do list for future efforts in the apparent horizon tracker

- Speed up the level flow method.
- Parallelize the apparent horizon tracker.
- Integrate the level flow apparent horizon tracker into the evolution code.

Our collaborators at The Pennsylvania State University have preliminary results [16] of initial data for multiple black holes. We hope to track the apparent horizons for this initial data and to evolve the data soon. The work in this thesis will be directly applicable to the completed initial data set. Making the simulations run longer is extremely important to get at the

physics of the situation. Two pieces of information that will be important as we continue to improve the longevity of the binary black hole simulation are gravitational wave extraction and event horizon tracking. With this in mind, a current to-do list for the evolution code includes:

- Blend to single hole at the outer boundary.
- Blend to a spherical geometry.
- Push out outer boundary (requires parallel version).
- Refine resolution (requires parallel version).
- Use constraint satisfying initial data.
- Extract gravitational radiation.
- Track the event horizon.

Finally, a note on putting the pieces of the puzzle together. This work is a highly collaborative operation, with different pieces being developed by different groups. We remain in close collaboration and substantial steps toward putting the puzzle together are underway. Our current efforts will not give us the complete solution to the binary black hole merger problem, but we have already taken dramatic steps in that direction.

Bibliography

[1] AGAVE,

<http://www.astro.psu.edu/users/mijan/agave>.

[2] M. Alcubierre, S. Brandt, B. Bruegmann, C. Gundlach, J. Masso, E. Seidel and P. Walker, “Test beds and applications for apparent horizon finders in numerical relativity,” gr-qc/9809004.

[3] A. Anderson, J. York, Phys. Rev. Lett. **82**, 4384 (1999).

[4] P. Anninos, G. Gaeus, J. Masso, E. Seidel, L. Smarr, *Horizon Boundary Condition for Black Hole Spacetimes*, Phys. Rev. D **51**, 5562 (1995).

[5] Apparent Horizon Boundary Condition Workshop, Max-Planck-Institut für Gravitationsphysik, Germany.

[6] R. Arnowitt, S. Desner, C. Misner, in *Gravitation, and Introduction to Current Research*, edited by L. Witten, Wiley, New York (1962).

- [7] Binary Black Hole Grand Challenge Alliance, Nation Science Foundation.
- <http://www.npac.syr.edu/projects/bh/>
- [8] N.T. Bishop, *Gen. Rel. Grav.* **14**, 717 (1982).
- [9] K. Brakke, “The Motion of a Surface by its Mean Curvature”, *Mathematics Notes* **20**, Princeton Univ. Press, Princeton (1978).
- [10] N.T. Bishop, R. Gomez, L. Lehner, M. Maharaj, J. Winicour, “Highpowered Gravitational News”, *Phys. Rev. D* **56**, 6298 (1997).
- [11] D. Bernstein, *unpublished notes* (1993).
- [12] C. Bona, J. Masso, E. Seidel and J. Stela, “A New formalism for numerical relativity,” *Phys. Rev. Lett.* **75**, 600 (1995).
- [13] H. Bondi, M.G. van der Burg and A.W. Metzner, “Gravitational Waves In General Relativity. 7. Waves From Axisymmetric Isolated Systems,” *Proc. Roy. Soc. Lond.* **A269**, 21 (1962).
- [14] D.R. Brill, R.W. Lindquist, *Phys. Rev.* **131**, 471 (1963).
- [15] B. Bruegmann, “Binary Black Hole Merger in 3d Numerical Relativity”, *Int. J. Mod. Phys. D* **8**, 85 (1999).
- [16] K. Camarda, *Ann. of Phys.* To Be Published.
- [17] Cactus Code

<http://www.cactuscode.org>

- [18] A. Cadez, “Apparent Horizons in Two BlackHole Problem”, *Ann. of Phys.* **83**, 449 (1974).
- [19] M. Choptuik, “Consistency of Finite-Difference Solutions of Einstein’s Equations,” *Phys. Rev.* **D44**, 3124 (1991).
- [20] M. Choptuik, “A Study of Numerical Techniques for Radiative Problems in General Relativity,” PhD Dissertation, University of British Columbia, (1986).
- [21] M. Choptuik, “The 3+1 Einstein Equations,” Relativity II Class Notes, University of Texas, (1998).
- [22] G.B. Cook *et al.* [Binary Black Hole Challenge Alliance], “Boosted three-dimensional black hole evolutions with singularity excision,” *Phys. Rev. Lett.* **80**, 2512 (1998).
- [23] G.B. Cook and J.W. York, “Apparent Horizons For Boosted Or Spinning Black Holes,” *Phys. Rev.* **D41**, 1077 (1990).
- [24] R. Correll, “Numerical evolution of Binary Black Hole Space-times,” PhD Dissertation, University of Texas, (1998).
- [25] K. Eppley, “Evolution Of Time Symmetric Gravitational Waves: Initial Data And Apparent Horizons,” *Phys. Rev.* **D16**, 1609 (1977).
- [26] L.S. Finn, *Gravitational Radiation Sources and Signatures*, gr-qc/9903107.

- [27] E.E. Flanagan and S.A. Hughes, “Measuring gravitational waves from binary black hole coalescences: 1. Signal-to-noise for inspiral, merger, and ringdown,” *Phys. Rev.* **D57**, 4535 (1998).
- [28] S. Frittelli, O. Reula, gr-qc/9904048.
- [29] M. Gage, R. Hamilton, *J. Diff. Geom.* **23**, 69 (1986).
- [30] R. Gomez, in Proceedings of “The Grand Challenge Alliance Fall Meeting,” Los Alamos, (1997).
- [31] R. Gomez *et al.*, [Binary Black Hole Challenge Alliance], “Stable characteristic evolution of generic three-dimensional single black hole space-times,” *Phys. Rev. Lett.* **80**, 3915 (1998).
- [32] M. Grayson, *The Heat Equation Shrinks Embedded Plane Curves to Round Points*, *J. Diff. Geom.*, **26**, 285 (1987).
- [33] C. Gundlach, “Pseudospectral apparent horizon finders: An Efficient new algorithm,” *Phys. Rev.* **D57**, 863 (1998).
- [34] S. Hawking, “Event Horizons”, in *Black Holes: Proceedings of the 23rd Les Houches Summer School*, edited by C. DeWitt, B. DeWitt, Gordon and Breach, New York (1973).
- [35] H. Freidrich, “Hyperbolic reductions for Einstein’s field equations,” *Class. Quant. Grav.*, **13**, 1451 (1996).
- [36] P. Hübner, *Class. Quant. Grav.*, **12**, 791 (1995).
- [37] G. Huisken, *J. Diff. Geom.* **20**, 237 (1984).

- [38] M.F. Huq, “Apparent Horizons in Numerical Spacetimes,” PhD Dissertation, University of Texas, (1996).
- [39] M. Huq, R. Matzner, *Binary Black Hole Grand Challenge Alliance Cauchy Code: The Documentation*, Unpublished (1998).
- [40] A.J. Kembal, N.T. Bishop, “The Numerical Determination of Apparent Horizons”, *Class. Quant. Grav.* **8**, 1361 (1991).
- [41] P. Laguna, *private communication*.
- [42] V.M. Lipunov, K.A. Postnov and M.E. Prokhorov, “First LIGO events: Binary black holes mergings,” astro-ph/9610016.
- [43] R.A. Matzner, M.F. Huq and D. Shoemaker, “Initial data and coordinates for multiple black hole systems,” *Phys. Rev.* **D59**, 024015 (1999).
- [44] Max-Planck-Institut für Gravitationsphysik, Germany, Binary Black Hole Grazing Collision,

<http://www.ncsa.edu>.
- [45] C. Misner, K. Thorne, J. Wheeler, *Gravitation*, W.H. Freeman and Co., New York, (1970).
- [46] T. Nakamura, Y. Kojima, K. Oohara, “A Method of Determining Apparent Horizons in Three-Dimensional Numerical Relativity”, *Phys. Lett.* **106A**, (1984).
- [47] S. Osher, J. Sethian, *J. Comp. Phys.* **79**, 12 (1988).

- [48] E. Pasch, *SFB 382* Report Number **63** (1997).
- [49] R. Penrose, *Phys. Rev. Lett.* **10**, 66 (1963).
- [50] L. Petrich, S. Shapiro, S. Teukolsky, *Phys. Rev. D* **31**, 2459 (1985).
- [51] W. Press, S. Teukolsky, W. Vetterling, B. Flannery, *Numerical Recipes*, Cambridge University Press, Cambridge, 1986.
- [52] R.K. Sachs, *Proc. Roy. Soc. Lond.*, **A270**, 103 (1983).
- [53] B. Schutz, *Geometrical Methods of Mathematical Physics*, Cambridge University Press, Cambridge (1980).
- [54] K. Schwarzschild, *Math.-Phys. Tech.*, 189 (1916).
- [55] E. Seidel, W. Suen, *Phys. Rev. Lett.*, **69**, 1845 (1992).
- [56] D. Shoemaker, in “The Grand Challenge Alliance Fall Meeting,” Austin (1998).
- [57] S.A. Teukolsky, *Unpublished* .
- [58] J. Thornburg, *Class. Quant. Grav.*, **4**, 1119 (1987).
- [59] J. Thornburg, “Finding apparent horizons in numerical relativity,” *Phys. Rev.* **D54**, 4899 (1996).
- [60] K.P. Tod, “Looking for Marginally Trapped Surfaces”, *Class. Quant. Grav.* **8** L115 (1991).

- [61] A.V. Tutukov, L.R. Yungelson, *Mon. Not. Roy. Astro. Soc.*, **260:675** (1993).
- [62] R. Wald, *General Relativity*, The University of Chicago Press, Chicago, (1984).
- [63] J. York, “Kinematics and Dynamics in General Relativity”, *Sources of Gravitational Radiation*, edited by L. Smarr, Cambridge Univ. Press (1979).
- [64] J. York, *Frontiers in Numerical Relativity*, edited by C.R. Evans, L.S. Finn, D.W. Hobill, Cambridge University Press, Cambridge (1989).

Vita

Deirdre Marie Shoemaker was born in Philadelphia, Pennsylvania on December 19, 1971, the daughter of Anne Durkin Shoemaker and Harry Shoemaker. She completed her secondary education at Council Rock High School in Newtown, Pennsylvania in 1990 and then entered the Pennsylvania State University as a dual physics and astronomy and astrophysics major. She earned her Bachelor of Science with honors in December of 1994 and entered graduate school at the University of Texas at Austin Department of Physics in August 1995.

Permanent Address: P.O. Box 179
Boalsburg, PA 16827

This dissertation was typeset with $\text{\LaTeX} 2_{\epsilon}$ ¹ by the author.

¹ $\text{\LaTeX} 2_{\epsilon}$ is an extension of \LaTeX . \LaTeX is a collection of macros for \TeX . \TeX is a trademark of the American Mathematical Society. The macros used in formatting this dissertation were written by Dinesh Das, Department of Computer Sciences, The University of Texas at Austin.